https://doi.org/10.26599/FRICT.2026.9441340

Research Article

Investigation on the anti-friction performance of ink sac-inspired textures under heavy-load conditions

Junyang Shang[1], Tianyi Tang[1], Chengxu Zhang[2], Kai Zhang[1,2] ✉, Kai Feng[1,2]

[1] Hunan Provincial Key Laboratory of Components for Frontier Equipment, 17, Changsha,410082, China

[2] Mechanical Industry Engineering Research Center for Fluid Lubricated Bearings, Hunan University, Changsha,410082, China

✉*Corresponding author. E-mail:* zhangkai04061121@163.com

Received: July 15, 2026; Revised: November 5, 2026; Accepted: November 18, 2026

© The Author(s) 2026.

Just Accepted

Abstract: The working surfaces of PEEK-coated sliding bearings in wind turbines are highly susceptible to severe friction and wear under specific operating conditions of low-speed and heavy-load. To improve the lubrication at the working interface, this paper proposes a novel textured structure inspired by the ink sac structure of cephalopods, adapted to the operating conditions and substrate materials of wind turbines. This new texture utilizes the significant deformation of the PEEK layer to transport lubricant, mimicking the ink-ejection behavior of cephalopods. Samples featuring this novel

surface texture were fabricated using 3D printing technology, and a friction and wear test rig was constructed to verify its outstanding anti-friction performance. Under test conditions with the lowest rotational speed and the heaviest load, the coefficient of friction was reduced by 18% compared to that of a smooth specimen. A high-speed camera was used to capture the lubricant delivery process of the new texture under heavy-load conditions. The results demonstrate that the proposed texture exhibits significant oil-squeezing effects; after the system started up in dry-friction state, the coverage of the oily area increased by 63%, and the average grayscale value increased by 18%. Furthermore, the effects of texture shape parameters, texture density, and initial surface oil volume on performance were analyzed. This paper provides a reference for the surface texture design of highly elastic friction components under heavy-load conditions.

Keyword: Heavy-Load; PEEK; Biomimetic textures; Friction and wear test rig.

Just Accepted

1 Introduction

Large wind turbines are currently widely used as clean energy equipment, and sliding bearings, which serve as the main shaft support units, are the core components of the turbine's power transmission system [1]. During the operation of a wind turbine, the sliding bearings must support the weight of the main shaft, blades and other components, which amounts to hundreds of metric tons, as well as complex wind loads [2]. However, wind turbines generally face extremely harsh operating conditions, such as low-speed, heavy-load operation and frequent starts and stops, which can easily degrade the lubrication condition at the friction pair interface of bearings [3]. At the same time, the PEEK coating on the bearings undergoes significant elastic deformation under high contact loads, further exacerbating interface friction and material wear, significantly shortening the service life of the sliding bearings, and directly affecting the stable operation of the wind turbine. Therefore, it is crucial to implement appropriate friction-reduction measures to address the issues of severe friction and wear

at the bearing contact surfaces.

Surface texturing, as an efficient surface modification and friction-reduction technique, is widely used on the working surfaces of equipment. The primary friction-reducing mechanisms recognized by many scholars include the additional hydrodynamic pressure effect, the secondary lubrication effect, and the reservoir effect [4-7].

Many researchers have conducted tribological studies on PEEK and other polymer materials to investigate the various lubrication mechanisms associated with surface texture under different lubrication conditions [8-19]. Harris et al. [20] investigated the hydrodynamic pressure and friction forces in a reciprocating sliding pair made of polyetheretherketone (PEEK) polymer, focusing on the effects of circular surface texturing. They examined the effects of surface textures diameter and depth on friction reduction, achieving a maximum reduction in the coefficient of friction of 48.7%. Wang et al. [21] used a picosecond laser to fabricate circular pit textures on PEEK surface. They proposed that the circular texture on the PEEK surface could trap PEEK abrasive particles generated during the friction process, reducing abrasive wear caused by free abrasive particles. Gheisari et al. [22] investigated the effect of texture on the tribological properties of aromatic thermosetting copolyester (ATSP) and ultra-high molecular weight polyethylene (UHMWPE) under low-oil lubrication conditions. They attributed the role of the texture to lubricant retention capacity and pointed out that surface micro-pits could serve as microscopic lubricant reservoirs, replenishing the lubricant when it is insufficient. Most of the aforementioned studies have focused on regularly shaped textures, thoroughly illustrating the mechanisms and processes by which textures function under polymer-based conditions, thereby providing guidance for designing textures under similar conditions.

In recent years, textural design methods that draw on the biological structures and behaviors

Just Accepted

found in nature have provided important inspiration and guidance for designing texture with superior performance. Su et al. [23] bionically designed a parabolic weave based on the parabolic grooves on the squid bone, and the shape of the weave showed better load-bearing capacity. Wang et al. [24] fabricated a biomimetic texture on a CFRPEEK surface, inspired by the non-smooth, pitted morphology of mollusk surfaces. With appropriate parameters set, the biomimetic texture can effectively reduce the coefficient of friction and minimize wear. These studies indicate that selecting suitable organisms as prototypes based on specific application scenarios has become a reliable method for designing texture structures.

However, in wind power applications, the low-speed, heavy-load operating conditions and frequent start-stop cycles mean that bearings in wind turbines are constantly subjected to poor lubrication conditions, such as mixed lubrication and boundary lubrication. Therefore, there is an urgent need to develop a surface texture structure that can effectively address these harsh lubrication conditions while providing excellent wear-reducing properties. Specifically, the heavy-load operating conditions require the surface texture to possess large oil-storage capacity to ensure a more reliable and sustained oil supply under the harsh conditions of large-scale wind turbines. At the same time, the texture should enable a smooth and rapid oil supply response to improve lubrication conditions at the friction interface. It is worth noting that marine cephalopods possess the physiological ability to store and eject ink; when threatened by predators, they can release large amounts of ink in a short period of time. This is primarily due to the structure of their ink sacs, which can rapidly and significantly deform under muscular pressure. This characteristic aligns well with the surface texture requirements for PEEK-based sliding bearings in wind turbines; therefore, the structure of cephalopod ink sacs deserves special attention.

Just Accepted

Cephalopods such as cuttlefish, squid, and octopuses eject ink when threatened so as to escape. The ink rapidly forms a cloud in the water [25]. This cloud resembles a cephalopod in shape and size, serving to confuse predators and buy more time for escape. The composition of the ejected ink is unique; it is a mucus that disperses in water and contains irritants. This produces effects such as visual deception and chemical defense [26,27]. Bartol et al. [28] indicate that the instantaneous ejection velocity of squid can reach up to 2.0 m/s. Jiang et al. [29] found that a cuttlefish weighing a squid weighing only 20 grams expels 90% of the ink from its ink sac, approximately 800 milligrams, over the course of three ink-ejection events. The rapid and sufficient liquid squeezing effect of the ink sac can be an excellent mimic prototype for the texture structures of PEEK bearings which are applied in heavy-load and low-speed scenarios where obvious deformation exist.

In this study, a novel millimeter-scale biomimetic surface texture inspired by deep-sea cephalopods is proposed to improve the tribological performance of components operating under low-speed and heavy-load conditions. The longitudinal cross-sectional geometry of the texture is inspired by the structural characteristics of the cephalopod ink sac and, in particular, by its deformation-mediated fluid ejection mechanism. By translating this biological principle into surface-texture design, the proposed structure enables pre-stored lubricant to be expelled toward the sliding interface through pressure-induced cavity deformation, thereby providing lubricant replenishment under severe operating conditions. Finite element simulations were performed to quantify the deformation and associated volume variation of different texture geometries under high contact pressure, revealing their distinct lubricant-release capabilities. A high-speed camera was further employed to visualize the migration and redistribution of lubricant during sliding, providing experimental evidence for the lubricant replenishment mechanism. The friction-reduction performance of the proposed texture was

Just Accepted

subsequently evaluated using a custom friction and wear test rig. In addition, the effects of key parameters, including texture density, initial lubricant supply, texture geometry, load, and rotational speed, were systematically investigated. The results provide a mechanistic basis and practical design guidance for fabricating lubricant-storing and replenishing surface textures on compliant polymer substrates, particularly for tribological applications involving low-speed and heavy-load conditions.

2 Structural design and simulation

2.1 Design of ink sac-inspired textures

Under low-speed and heavy-load conditions, the contact interface predominantly operates in the mixed or boundary lubrication regime. Consequently, the additional hydrodynamic pressure caused by the texture is weakened, while lubricant storage and replenishment become the dominant lubrication mechanisms. From a design perspective, the texture geometry should therefore be optimized to maximize the efficiency of lubricant storage, release, and transport, while preserving adequate debris-trapping capacity to mitigate third-body abrasion.

Ink-ejection behavior in marine cephalopods is believed to be an adaptive mechanism that cephalopods use to defend themselves against predators [30]. Structurally, the ink sac primarily consists of ink glands and sphincter muscles. When stimulated by external factors, the sphincter contracts voluntarily, squeezing the ink sac and ejecting a large amount of ink through the ink duct, as depicted in Fig. 1a.

Figure 1a illustrates the defensive process of cephalopods when faced with predators. As shown in the figure, cephalopods detect the threat of a predator through sight and taste. They then adjust their body posture to aim their siphon at the predator, contract their muscles to squeeze the spindle-shaped

Just Accepted

ink sac, and eject ink. The ink rapidly forms a cloud in the water, confusing the predator. At the same time, this ejection provides the cephalopod with a certain amount of thrust, aiding its escape [31].

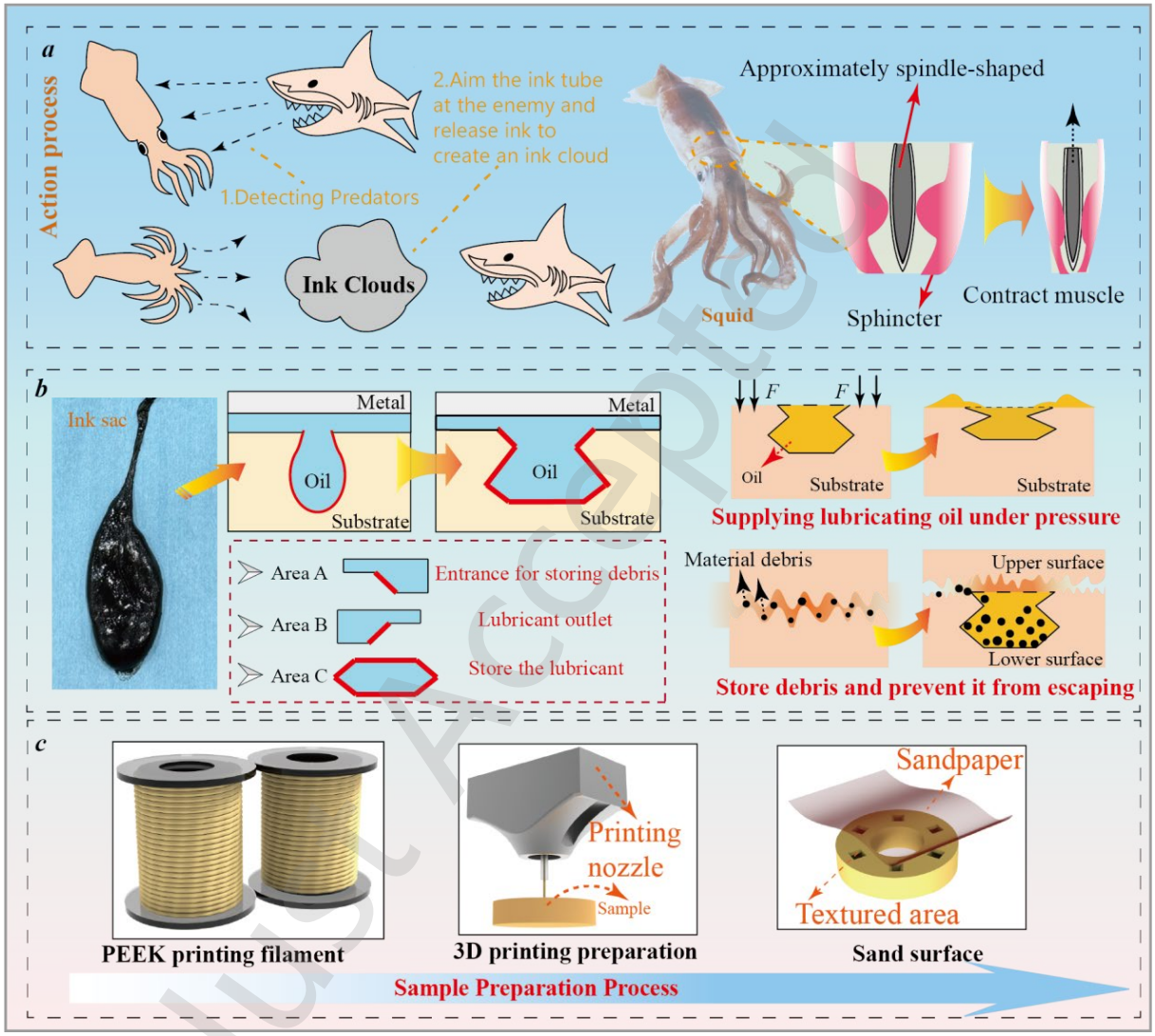


Fig. 1 Schematic diagram of surface textures inspired by the structure of cephalopods. (a) schematic diagram of cephalopods defending themselves against predators and changes in their ink sacs during the process. (b) actual photographs of ink sacs and texture structures, and the mechanism by which they reduce friction. (c) the process of preparing surface textures.

Figure 1b shows a photograph of the actual structure of a cephalopod ink sac and the biomimetic textured structure proposed in this paper. Two key issues have been identified. Issue 1: In the case of

the ink sac, the driving force during ink ejection is primarily horizontal, generated by muscle contraction. As shown in Fig. 2, the force F_{mus} here forces the ink sac to compress toward the center, ejecting the ink. However, when the texture structure is in operation, it primarily bears forces from the vertical plane of motion, resulting in a nearly 90° shift in the line of force between the two. Issue 2: In cephalopods, the ink sac serves solely to store ink; once ink is expelled, glands produce more ink to refill the sac. In contrast, the design of a texture structure must account for both the outward extrusion of oil and the inward accumulation of debris within the cavity. Due to the opposing movements of lubricant extrusion and debris ingress within the structure, its actual operational behavior differs significantly from that of an ink sac.

Table 1 Parameters of biomimetic texture

Item	Value
Inlet and outlet height, $h_{1\text{-shape1}}, h_{1\text{-shape2}}, h_{1\text{-shape3}}$	400 um, 400 um, 400 um
Main abdominal cavity height, $h_{2\text{-shape1}}, h_{2\text{-shape2}}, h_{2\text{-shape3}}$	800 um, 600 um, 800 um
The “neck” length, $l_{1\text{-shape1}}, l_{1\text{-shape2}}, l_{1\text{-shape3}}$	1200 um, 1040 um, 614 um
Bottom length, $l_{2\text{-shape1}}, l_{2\text{-shape2}}, l_{2\text{-shape3}}$	1200 um, 1600 um, 2710 um
The “neck” angle, $\varphi_{1\text{-shape1}}, \varphi_{1\text{-shape2}}, \varphi_{1\text{-shape3}}$	90°, 90°, 60°
Main abdominal cavity angle, $\varphi_{2\text{-shape1}}, \varphi_{2\text{-shape2}}, \varphi_{2\text{-shape3}}$	135°, 135°, 150°
Bottom angle, $\varphi_{3\text{-shape1}}, \varphi_{3\text{-shape2}}, \varphi_{3\text{-shape3}}$	45°, 45°, 30°

In light of these two issues, and considering the primary mechanisms of secondary lubrication and the reservoir effect in the structure, we realized that designing the structure based on the actual shape of an ink sac might fail to fully utilize its anti-wear performance. Therefore, the biomimetic geometry was further modified on the basis of the ink-sac morphology to better accommodate the

Just Accepted

actual loading and sliding conditions. To address Issue 1, and taking into account that the textured structure is primarily subjected to normal loads in practical applications, we designed a narrow-neck region for the structure. Under normal loads, deformation will concentrate in the narrow-neck region due to its low stiffness. This causes the volume inside the textured structure's cavity to be rapidly compressed, forcing the lubricant stored within it out. Meanwhile, the design of the large cavity beneath the textured structure increases the maximum amount of lubricant that can be stored inside it. To address Issue 2, the upper portion of the texture was designed as a trapezoidal channel with a wider opening and a narrower interior section from the perspective of wear-debris accommodation and lubricant transport. The primary benefits are that debris can flow more smoothly into the cavity through one side, while through the other side, lubricant is more effectively transported to areas with insufficient lubrication during relative motion. Additionally, to reduce the directional dependence of the structure, the outlets are symmetrically arranged on both sides. Furthermore, to ensure that debris stored within the structure is securely retained in the internal cavity, the bottom of the cavity is designed with straight edges and sharp corners. The specific design process is as follows:

(1) In order to enhance the ability of the texture to transport lubricant, area A employs a ramp design with a small inlet and a large outlet. This primarily enables the texture to better store oil when the friction surface under steady-state sliding conditions. Simultaneously, it facilitates the migration of wear debris generated on the friction surface into the texture's internal cavity.

(2) To increase the texture's capacity to retain debris, area B features a design with a small inlet and a large outlet. This ensures that lubricant flows more smoothly from the interior cavity of the texture to the working surface.

(3) To enhance the pre-lubrication capacity of the texture and ensure compatibility with large-

Just Accepted

scale equipment, the texture was designed with millimeter-level dimensions. Drawing inspiration from the structure of an ink sac, the volume of area C was increased. This provides greater potential for improvement under harsh surface lubrication conditions.

(4) The biomimetic texture is parameterized by a set of geometric dimensions, including the neck length l_1, bottom length l_2, inlet and outlet height h_1, main cavity height h_2, neck angle φ_1, main cavity angle φ_2, and bottom angle φ_3. These geometric parameters can be adjusted according to specific operating conditions and application requirements. By varying the above parameters, this paper obtained shape1-3, and their specific parameters are listed in Table 1.

(5) To fully achieve the secondary lubrication effect, a narrow neck structure is designed near the top of the longitudinal cross-section. Under normal loading, the relatively compliant PEEK substrate allows the neck region to undergo localized deformation, thereby reducing the effective cavity volume and promoting lubricant transport from the internal cavity toward the sliding interface. During unloading, partial elastic recovery of the cavity may further facilitate lubricant redistribution and replenishment.

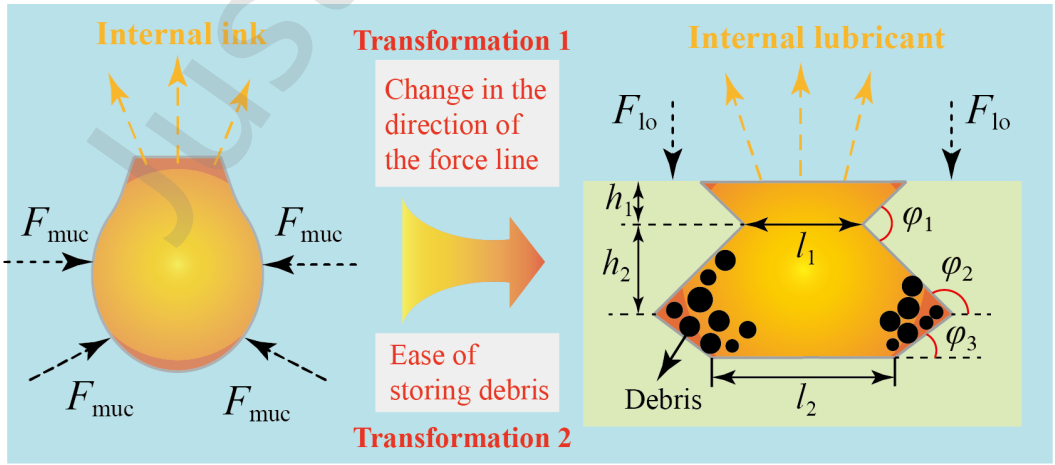


Fig. 2 Schematic diagram of mechanism analysis and shape evolution.

Figure 1b also illustrates the primary mechanisms of action of the fabric under low-speed, heavy-

Just Accepted

load conditions, namely the secondary lubrication mechanism and the reservoir mechanism [32]. First, regarding the secondary lubrication mechanism, the texture possesses a certain internal cavity volume, giving it the ability to store lubricant. When pressure is applied to the working surface, the texture deforms, causing its internal volume to shrink. The lubricant previously stored within is squeezed out and, driven by the relative motion of the surfaces, is transported to the oil-starved areas of the working surface, thereby ensuring timely replenishment when lubricant is insufficient. Second, regarding the reservoir mechanism: under specific operating conditions of low-speed and heavy-load, debris shed from the upper and lower surfaces of the mating parts due to wear is carried between the working surfaces. Resulting in three-body wear between the working surfaces, which can lead to severe wear issues. After introducing the textured structure, the cavities within the texture accommodate a certain volume of debris, reducing the likelihood of debris remaining in the contact interface and participating in further abrasion. This contributing to improved tribological performance, and due to the storage pool effect of the texture, it also helps reduces surface damage.

Figure 1c illustrates the fabrication process of the textured specimens. Owing to the relatively large texture dimensions and the presence of complex internal cavities, conventional surface-texturing methods are not suitable for fabricating the proposed structures. Additive manufacturing offers greater geometric flexibility for producing components with complex internal features [33,34]. For metallic components, commonly used additive-manufacturing techniques include powder bed fusion and direct metal laser sintering [35]. In the present study, however, PEEK was selected as the substrate material. Considering its thermoplastic nature and the geometric complexity of the biomimetic texture, fused deposition modeling (FDM) was employed to fabricate the specimens. PEEK filament was heated above its melting temperature, extruded through the printer nozzle, and deposited layer by layer to

Just Accepted

form the designed texture geometry. The fabricated PEEK specimen is shown in Fig. 7. Because the dimensional accuracy and surface quality achievable by FDM are limited, subsequent processing was performed to ensure that the specimens satisfied the dimensional and surface-quality requirements of the tribological tests. Due to the inherent defect of low processing accuracy in 3D printing technology, in order to meet the requirements of experimental accuracy, the PEEK sample was ground using the target sandpaper. Use sandpaper of 800 mesh, 1000 mesh and 4000 mesh respectively in the order of use for grinding. Finally, the roughness was ground to Ra 1.6um for the friction and wear test.

In summary, the ink sac inspired biomimetic texture proposed in this study exhibits several potential tribological advantages:

(1) **Enhanced secondary lubrication effect.** Compared to traditional texture shapes, the cephalopod-inspired biomimetic texture utilizes its tapered structure—narrower at the top and wider at the bottom—to facilitate promotes load-induced deformation and lubricant release through the "neck" structure to the exterior under normal loading. Simultaneously, the inclined ramp design at the inlet and outlet facilitates internal oil storage within the texture and efficient delivery of lubricant to friction surfaces. This unique biomimetic design contributes to reduced friction under the investigated low-speed and heavy-load conditions.

(2) **Enhanced lubricant storage and debris accommodation.** The inlet design of the cephalopod-inspired structure enables more efficient debris capture when the working surface experiences severe wear. Simultaneously, the narrow neck structure ensures that retained wear debris is largely retained within the structure, significantly reducing the amount of debris on the surface. This reduces the participation of loose debris in interfacial abrasion and thereby mitigates three-body abrasive wear. From the perspective of the texture's reservoir effect, this biomimetic texture

Just Accepted

represents a preferred choice for surface anti-friction design in low-speed, heavy-load operating conditions.

(3) **Potential applicability to large-scale components.** Compared to traditional micron-scale textures, the millimeter-scale texture proposed in this paper provides a larger lubricant-storage capacity within each individual texture. Under mixed or boundary lubrication conditions, the stored lubricant can be released from the internal cavity toward the sliding interface, thereby contributing to lubricant replenishment when the local lubricant supply becomes insufficient. This characteristic may be advantageous for large-scale tribological components operating under low-speed and heavy-load conditions, where maintaining an adequate lubricant supply over an extended contact area is particularly important.

(4) **Fabrication flexibility for complex geometries.** Additive manufacturing provides a convenient approach for fabricating PEEK specimens containing millimeter-scale textures with complex internal geometries. Compared with conventional subtractive machining, fused deposition modeling (FDM) allows features such as the narrow neck and internal cavity to be formed directly without requiring multiple machining steps. This capability facilitates the fabrication and geometric modification of different texture designs during the structural optimization process.

2.2 Numerical simulation and analysis

Finite element analysis was conducted using ANSYS to investigate the deformation behavior of different textured PEEK structures under external loading and to evaluate the associated changes in cavity volume. As shown in Fig. 3, in order to better align with the actual engineering scenarios, a uniform pressure of 80 MPa was applied to represent the heavy-load condition considered in the simulation. Among the investigated geometries, Shape3 exhibited the largest deformation, whereas the

Just Accepted

rectangular texture and Shape2 showed comparatively smaller deformation. These results indicate that the deformation response of the PEEK texture is strongly dependent on its geometric configuration. After completing the simulation, the volume change of the structures with different shapes before and after compressive deformation was calculated by measuring the volume of the internal cavity.

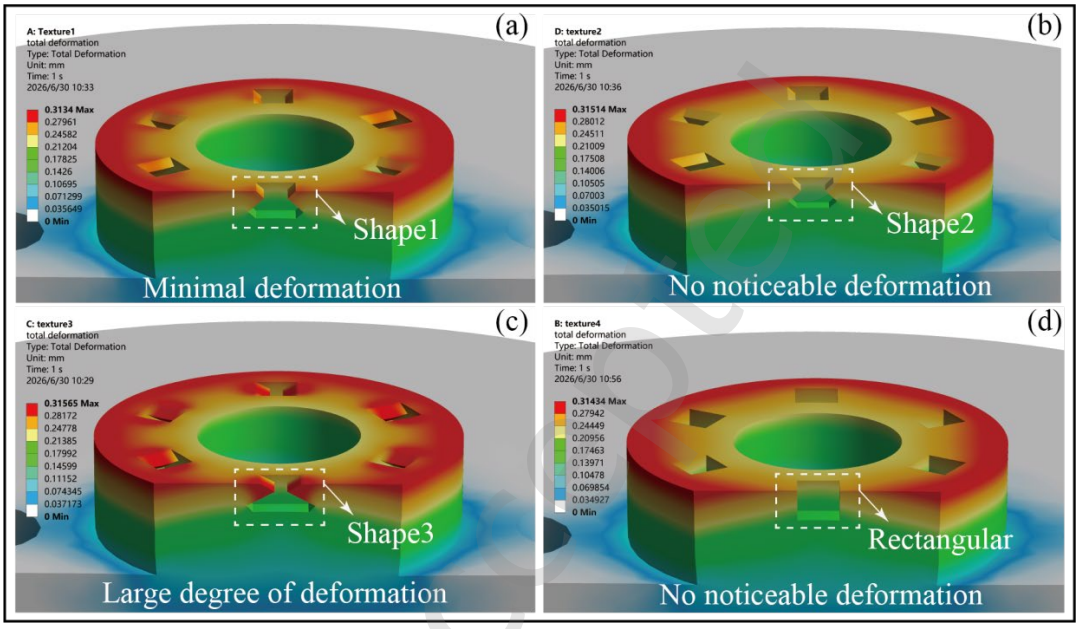


Fig. 3 Deformation simulation under static pressure. (a) texture shape1 deformation. (b) texture shape2 deformation. (c) texture shape3 deformation. (d) rectangular texture deformation.

As shown in Fig. 4, Shape2 exhibits the smallest cavity-volume change under heavy loading, with a value of only 0.072 mm^3 . In contrast, Shapes1 and Shapes3 exhibit relatively larger volume changes after compression. Compared with the conventional rectangular texture, the volume change of Shape1 is 56.86% greater, while that of Shape3 is 45.20% greater than that of Shape1. These results indicate that the proposed biomimetic textures, particularly Shape3, exhibit a stronger deformation response under the same loading condition, resulting in a larger variation in internal cavity volume. A larger cavity-volume change indicates a greater potential for load-induced lubricant release. However, it should not be interpreted as necessarily leading to superior lubrication performance, because excessive deformation may also cause stress concentration or structural instability. Therefore, cavity-volume

Just Accepted

variation should be considered together with lubricant storage, structural integrity, and interfacial lubricant transport when evaluating the lubrication performance of the texture.

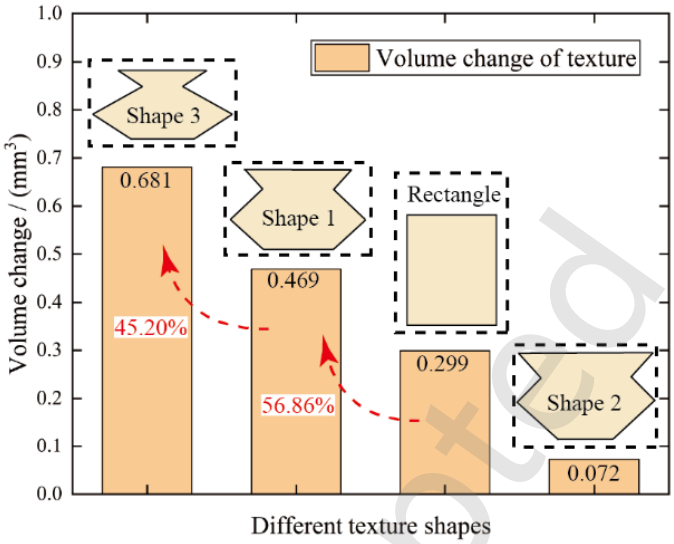


Fig. 4 Absolute cavity volume reduction of different texture shapes under external loads.

The results in Fig. 4 show that Shape3 exhibits the highest absolute cavity volume reduction, indicating that it provides the best oil-ejection performance under the same external load conditions. This is because Shape3 has the smallest geometric diameter and the smallest angle at its narrow neck; when an external force is applied, the side walls at the bottom of Shape3 are more inclined, resulting in a stronger tendency toward radial contraction. At the same time, the narrow-neck design of Shape3 causes the internal cavity structure to collapse toward the orifice under external force, thereby generating greater deformation. In contrast, Shape2 has a larger orifice size, which weakens the concentration effect of the external force at the orifice. Furthermore, its gentler sidewall profile reduces the tendency for radial contraction. Consequently, even under identical external load conditions, Shape2 exhibits less overall deformation and a smaller absolute cavity volume reduction. Compared to Shape2 and traditional rectangular shapes, Shape1 offers certain advantages in terms of absolute cavity volume reduction.

Just Accepted

In addition, to further illustrate the advantages of the narrow-neck, he dimensionless cavity contraction ratio is defined as follows:

$$\eta = \frac{V_0 - V_L}{V_0} = \frac{\Delta V}{V_0} \tag{1}$$

Where the V_0 is volume of the cavity before deformation, V_L is volume after deformation. Since the lubricant is treated here as an incompressible fluid, the volume of lubricant displaced is primarily determined by the decrease in the chamber volume:

$$V_{out} = \Delta V \tag{2}$$

The calculation results are shown in Table 2, it can be seen here that the biomimetic texture structure proposed in this paper, while featuring a large cavity volume, also exhibits a higher cavity contraction ratio due to its narrow-neck design. This result also confirms that increasing the proportion of the narrow-neck region, as seen when comparing Shape3 to Shape1, approximately doubles the cavity contraction ratio.

Table 2 Dimensionless volume contraction ratio calculation results

Texture shape	Initial cavity volume	Cavity contraction ratio η	Absolute cavity volume reduction
Shape1	7.360 mm^3	0.0637	0.469 mm^3
Shape2	4.029 mm^3	0.0179	0.072 mm^3
Shape3	5.343 mm^3	0.1275	0.681 mm^3
Rectangle	3.200 mm^3	0.0934	0.299mm^3

As shown in Table 2, Shape2 has a lower cavity contraction ratio, and the absolute cavity volume reduction is also smaller than that of the rectangular texture. In contrast, while the cavity contraction ratio of Shape1 (0.0637) is lower than that of the rectangular texture (0.0934), its absolute cavity volume reduction reaches 0.469 mm^3, which is approximately 56.86% higher than that of the

Just Accepted

rectangular texture (0.299 mm^3). Shape 3 outperforms the rectangular texture in both cavity contraction ratio and absolute cavity volume reduction. This indicates that not all three biomimetic textures possess superior oil-squeezing performance.

However, from the above comparison, it can also be seen that from Shape2 to Shape1 and then to Shape3, the structural feature of the narrow neck combined with the large cavity gradually becomes prominent. The absolute cavity volume reduction has increased from 0.072 mm^3 to 0.469 mm^3 and 0.681 mm^3, respectively, and the cavity contraction ratio has increased from 0.0179 to 0.0637 and 0.1275, respectively. This trend indicates that the combination of a narrow neck and a relatively large cavity is more likely to produce greater cavity deformation under external loads, thereby increasing the volume of lubricant expelled from the texture. This demonstrates that the structural characteristics of the narrow-neck, large-cavity configuration offer significant advantages in enhancing oil-squeezing performance.

3 Experiment verification

3.1 Test rig and procedure

In this paper, a self-built end-face friction and wear test bench was used, as shown in Fig. 5 and Fig. 6. The test bench is equipped with a drive motor with a rated output torque of 5N·m, a rated power of 1 kW and a rated speed of 2000 rpm. Pressure transducers and tension transducers are arranged underneath the test bench to detect the applied load and the equivalent friction force, respectively. In addition, the test bench adopts the loading method of weight loading, and the loading force of different experimental conditions can be realized by adjusting the weight of the weight, and the lever ratio of the force arm of the loading torque is 1:10. Due to the friction, the sample, the oil cavity and the support

Just Accepted

shaft of the oil cavity are all connected by threads to form a rigid whole. The specific test bench and specimen parameters are shown in Table 3.

During loading, the torque-amplification lever pivots through a small angle about its fixed point, causing the rigid assembly to undergo a small vertical displacement. This displacement may introduce additional friction between the rigid assembly and the test rig. In addition, friction generated within the loading mechanism may produce a resisting torque opposite to the friction torque being measured. These effects can introduce additional errors into the measured friction torque and therefore reduce the measurement accuracy.

Table 3 Specific Parameters of the Test Bench

Item	Value
Air supply pressure of porous radial bearings, p_r	5 bar
The gas supply pressure of the small hole static pressure gas thrust bearing, p_t	5 bar
Length of the torque rod of the tension sensor, l	60 mm
Push force to float the diameter of the bearing, d_{Gas}	200 mm
Outer diameter of PEEK style, d_o	18 mm
Inner diameter of PEEK style, d_i	8 mm
Weight of Counterweights, G_W	2 N
Outer diameter of the pattern on the metal, d_{om}	60 mm
The maximum load-bearing capacity of the small hole static pressure gas thrust bearing, F_{max}	5500 N

Just Accepted

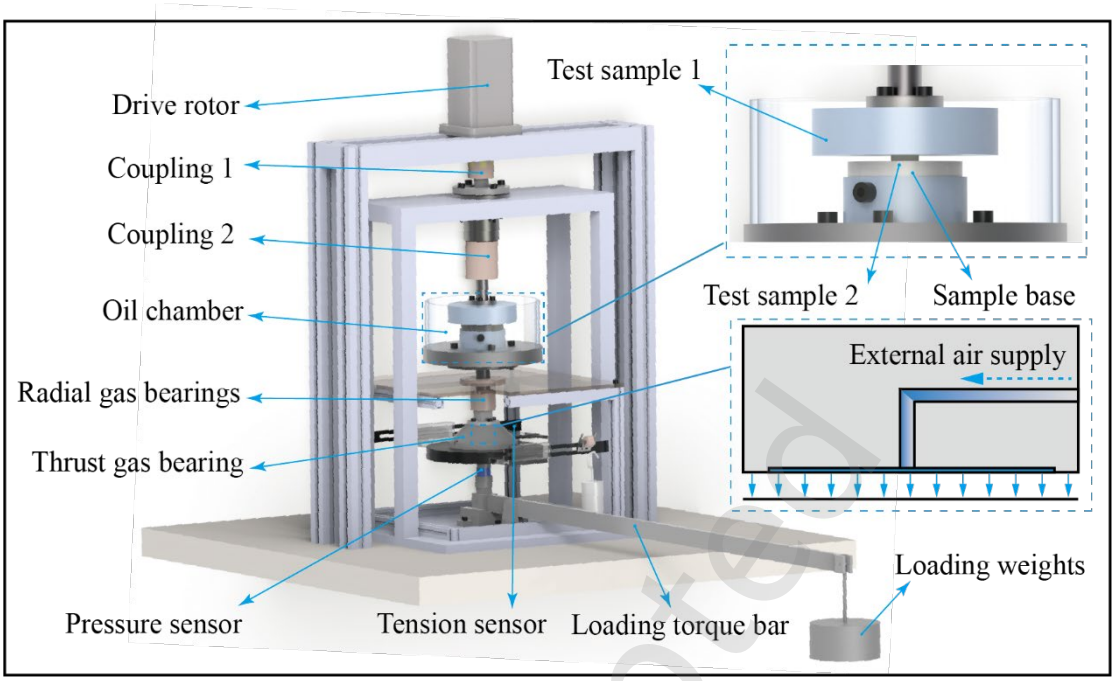


Fig. 5 The schematic diagram of the experimental bench.

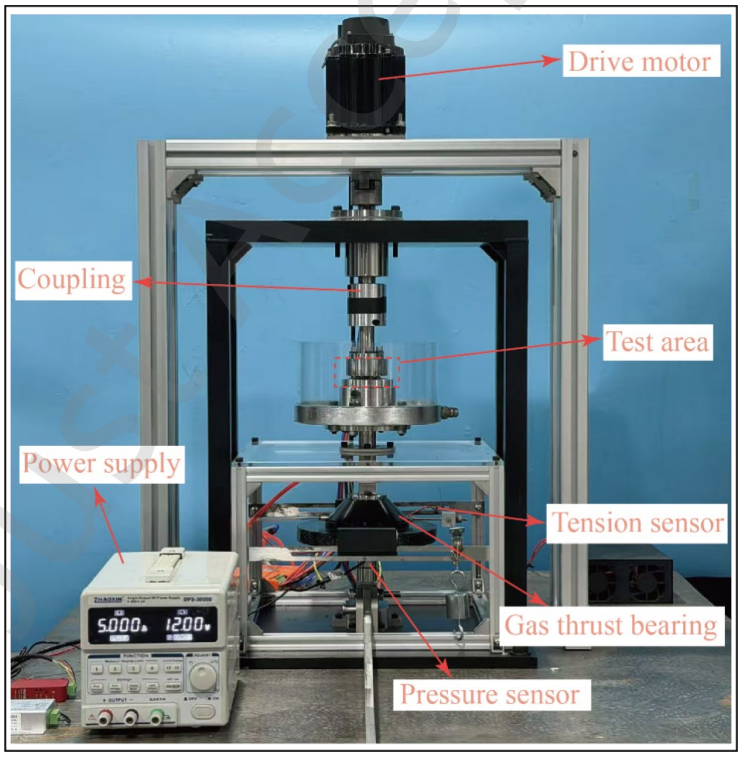


Fig. 6 The photograph of the experimental bench.

A multi-orifice radial gas bearing and a small-orifice thrust hydrostatic gas bearing were incorporated into the test rig. Using the small-orifice thrust hydrostatic gas bearing for load transfer eliminates additional friction in the loading zone, it is connected to tension sensor via a torque-

measuring rod. A counterweight is attached to the other end of the torque-measuring rod to ensure that the rod remains perpendicular to the tension sensor at all times. The use of porous radial gas bearings ensures the alignment of the rigid whole and the additional friction generated during up and down displacement, guaranteeing that no additional friction occurs on the transmission path of the frictional torque and ensuring the accuracy and reliability of the measurement results. The key parameter measured by the experimental bench is the coefficient of friction, which can be obtained through the calculation of Eq. (5) based on the principle of conservation of frictional torque.

To simulate the demanding lubrication conditions experienced by bearing components operating under low-speed, heavy-load conditions, a measured quantity of lubricating oil was injected onto the friction pair surfaces during the experiment. This replicated the operating state of mixed and boundary lubrication. The lubricating oil used in the experiment was Mobil SHC Gear 320WT, whose viscosity and density were 0.047 Pa·s and 0.89×10^3 kg/m³ respectively. The samples were cleaned with an ultrasonic cleaner before the experiments, and wiped with acetone and then dried. At the end of the experiment, the lower PEEK specimens samples were cleaned using an ultrasonic cleaner, wiped with acetone and dried. Surface micro-morphology characterization of worn PEEK specimens was performed using a super-depth-of-field microscope. Fig. 7 shows the samples used in the friction and wear test.

The measurement principle of test rig is as follows:

$$M_{\mathrm{f-a}} = M_{\mathrm{f-b}} \tag{3}$$

where the $M_{\mathrm{f-a}}$ is the frictional torque generated by the relative rotation of the frictional mating surfaces, the $M_{\mathrm{f-b}}$ is the frictional torque measured under the test bench through a tension sensor and other means.

Just Accepted

$$\begin{cases} M_{\mathrm{f}-a} = \mu F_{\mathrm{N}} \dfrac{r_{\mathrm{o}}^3 - r_{\mathrm{i}}^3}{r_{\mathrm{o}}^2 - r_{\mathrm{i}}^2} \\ M_{\mathrm{f-b}} = (F_{\mathrm{t}} - G_{\mathrm{W}})(l + r_{\mathrm{Gas}}) \end{cases} \tag{4}$$

$$\mu = \frac{F_{\mathrm{t}}(l + r_{\mathrm{Gas}})(r_{\mathrm{o}}^2 - r_{\mathrm{i}}^2)}{F_{\mathrm{N}}(r_{\mathrm{o}}^3 - r_{\mathrm{i}}^3)} \tag{5}$$

where the μ represents the friction coefficient of the friction pair surface and is also the main measurement target of the experimental bench in this paper, the F_{t} is the force measured by the tension sensor, the F_{N} is the loading force measured by the pressure sensor, the l is the torque measuring rod of the tension sensor, the r_{Gas} is the outer diameter of the air flotation thrust bearing.

Under the operating conditions of low-speed and heavy load, since a stable and continuous oil film has not been formed, when the two working surfaces come into contact, it is still mainly solid contact. At this time, the external load is mainly borne by rough peaks. To accurately determine the lubrication state, the Hamrock-Dowson formula is used for auxiliary explanation [36]. The minimum film thickness was approximately calculated by referring to the Hamrock-Dowson point contact formula. Based on the calculated film thickness ratio parameters, it can be determined that the lubrication state of the friction pair surface in this paper during operation is the boundary lubrication state. The calculation formula is as follows,

$$\lambda = \frac{h_{\min}}{\sigma^*} \tag{6}$$

$$h_{\min} = 7.43R(1 - 0.85e^{(-0.31k)})\left(\frac{\eta u}{(E^*)R}\right)^{0.65}\left(\frac{F_{\mathrm{N}}}{(E^*)R^2}\right)^{(-0.21)} \tag{7}$$

$$\sigma^* = \sqrt{\left(\sigma_{\mathrm{PEEK}}^2 + \sigma_{\mathrm{42CrMo}}^2\right)} \tag{8}$$

where the R is the composite radius, the η is the absolute viscosity, u is the mean sliding velocity, the E* is the composite elasticity modulus and the F_{N} is the normal loading force.

$$u = \frac{u_{\mathrm{PEEK}} + u_{\mathrm{42CrMo}}}{2} \tag{9}$$

Just Accepted

$$\frac{1}{E^*} = \frac{2}{\frac{1-\upsilon_{\mathrm{PEEK}}^2}{E_{\mathrm{PEEK}}} + \frac{1-\upsilon_{42\mathrm{CrMo}}^2}{E_{42\mathrm{CrMo}}}} \tag{10}$$

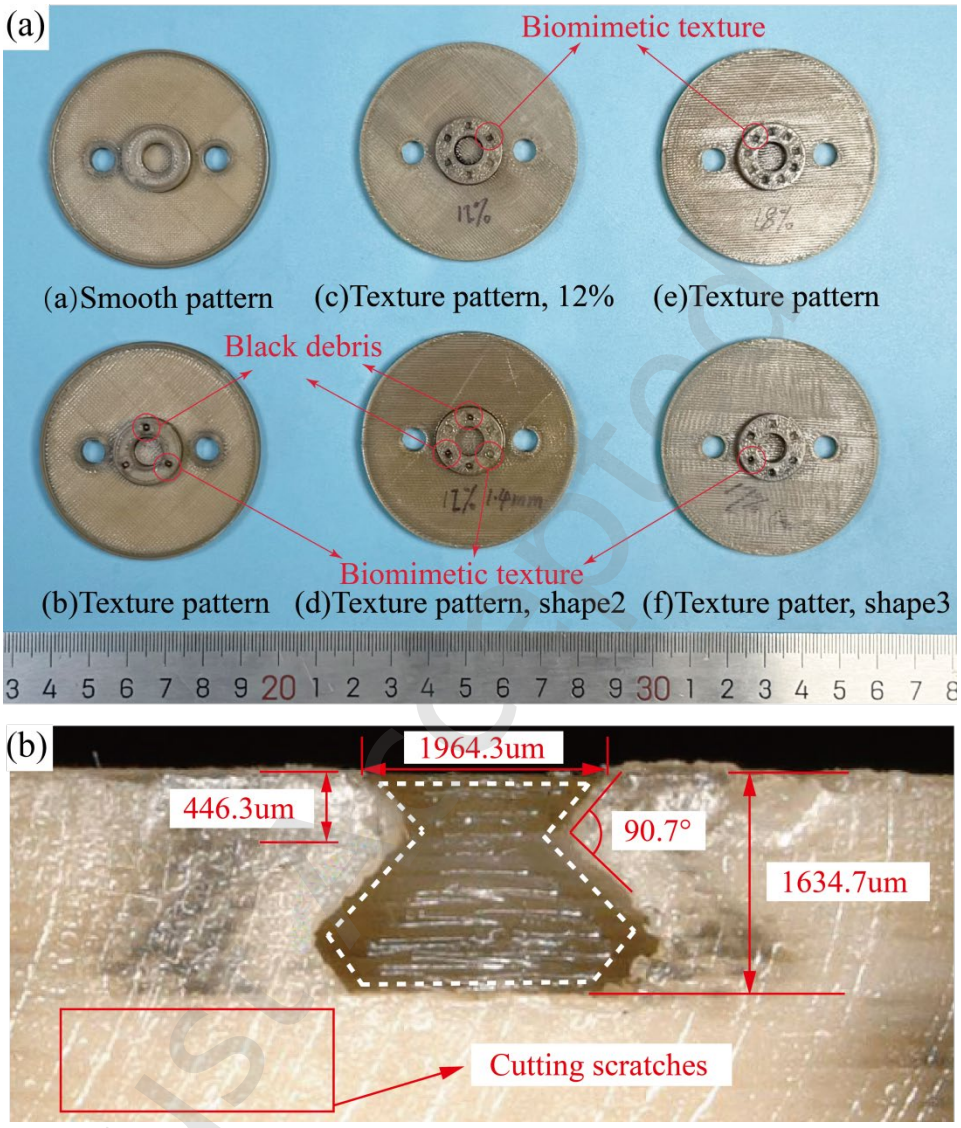


Fig. 7 PEEK-based experimental specimens. (a) schematic diagram smooth and texture pattern. (b) longitudinal profile of the texture.

Based on the film-thickness ratio calculated using the above equations and the corresponding lubrication-regime criterion, the friction pair investigated in this study was identified as operating predominantly under boundary-lubrication conditions. The detailed calculation procedure and classification criterion are provided in Appendix A.

3.2 Mechanism verification

To visually investigate the mechanism of lubricant release from textured under heavy loads, visualization experiments were conducted using a PEEK specimen with biomimetic texture pattern. Large-diameter PEEK samples with a ring-shaped texture were fabricated using 3D printing technology, and metal pins made of 42CrMo were prepared. Following a modified pin-on-disk configuration, the two metal pins were used as the upper specimen, and the textured PEEK specimen served as the lower specimen. The annular textured PEEK specimen used in the experiment is shown in Fig.8, and a schematic diagram of the experiment is shown in Fig. 9. A high-speed camera connected to a computer was used to continuously record the lubricant migration process, and auxiliary lighting was employed during filming.

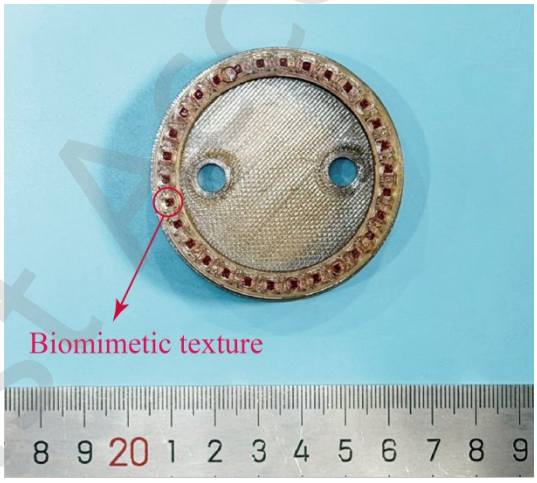


Fig. 8 PEEK sample for visualization photography.

In the characterization experiment, the annular surface of the PEEK-based sample was dry and filled with lubricant inside the texture. The experimental speed set for the characterization experiment is 10rpm and the load is 200N. The shooting results in Fig. 10 show that when the frame rate is 0ms and the rotational speed is 0, no obvious oil stains are observed on the surface of the sample. When the frame rate is 212ms, it can be observed that there are certain obvious oil stains in the area where

Just Accepted

the pin pattern has passed. This can prove that the texture contributes the lubricant stored in its inner cavity to the friction surface, and the lubricant squeezed out is distributed to the surface by the rotation of the pin pattern, achieving the purpose of wetting the surface. At a frame rate of 366ms, after the pin pattern passes through texture zone, a certain obvious oil stain can be seen in the non-texture area on the surface. When the frame rate is 1915ms, this is the second time that the pin pattern has passed through texture zone. It can be seen that more lubricant has accumulated in the non-texture areas on the surface, and the oil stains are more continuous.

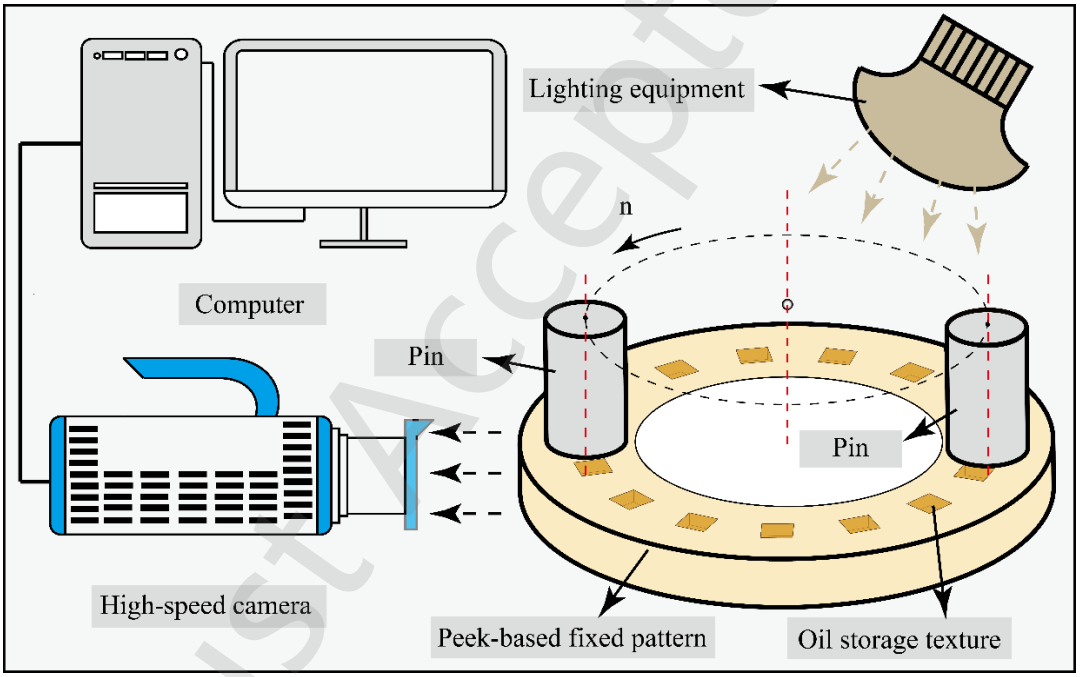


Fig. 9 Schematic diagram of the visual working principle.

Just Accepted

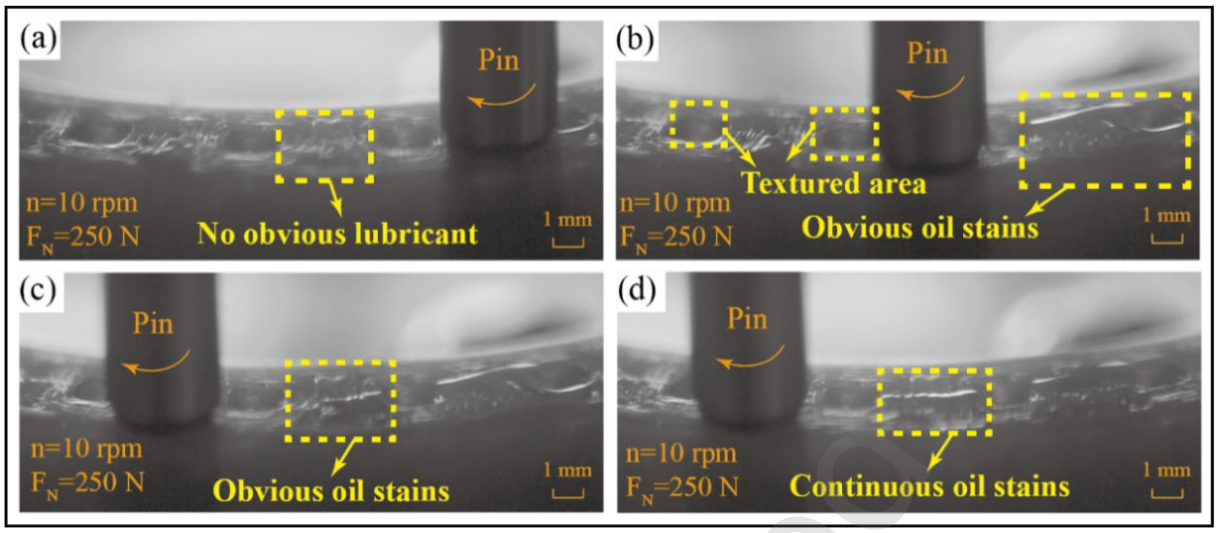


Fig. 10 Images captured by a high-speed camera at different times. (a) 0 ms.(b) 212 ms.(c) 366 ms.(d) 1915 ms.

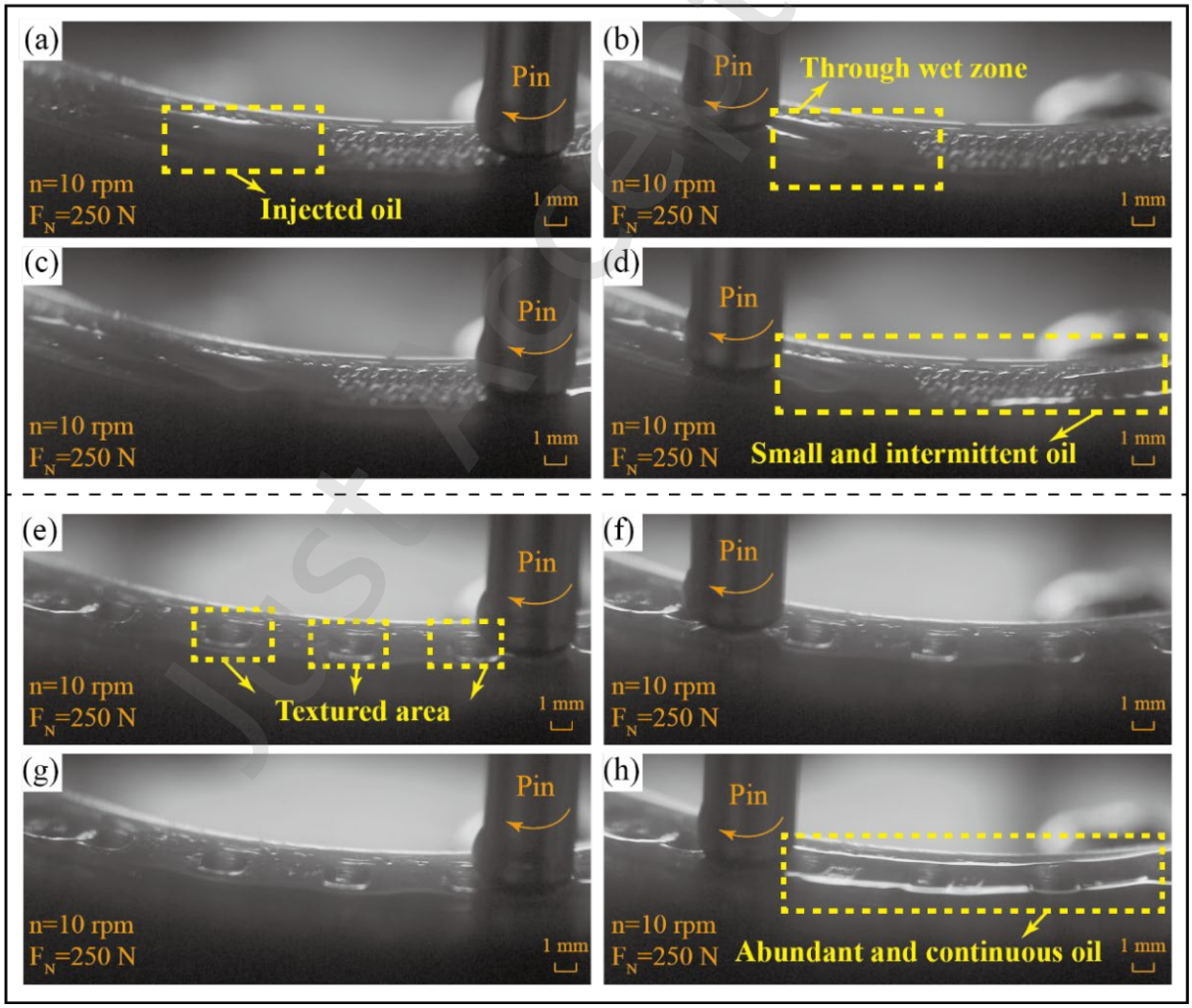


Fig. 11 Images captured by a high-speed camera at different times. (a) 0 ms. (b) 68 ms. (c) 3106ms. (d) 3728 ms. (e) 0 ms. (f) 632 ms. (g) 3000ms. (h) 3609ms.

Just Accepted

To visually demonstrate the contribution of surface texture to lubricant redistribution at the sliding interface, the same amount of lubricant was applied to both the smooth and textured PEEK specimens prior to the visualization experiments. Fig. 11a-d illustrate the lubricant migration behavior on the smooth PEEK surface. Before testing, 0.05 mL of lubricant was applied to the specimen surface. The two symmetrically positioned pins were designated as Pin 1 and Pin 2. Fig. 11a shows the initial state before sliding, with lubricant applied at the marked location and its symmetric counterpart. Fig. 11b shows Pin 1 passing through the lubricant-applied region. Fig. 11c shows Pin 2 reaching the initial position of Pin 1. Fig. 11d shows the lubricant trace in the region traversed by Pin 2; however, the lubricant distribution remains discontinuous.

Figures 11e–h illustrate the corresponding lubricant migration behavior on the textured PEEK surface under the same lubricant volume, rotational speed, and applied load. Fig. 11e shows the initial textured region, while Fig. 11f shows Pin 1 successively passing over the three textured cavities. Fig. 11g captures the subsequent motion of Pin 2 along the same sliding path. As shown in Fig. 11h, a more continuous lubricant trail forms behind the pin after it passes over the textured region. Comparison between Fig. 11d and Fig. 11h indicates that the textured surface promotes lubricant redistribution toward regions with insufficient lubricant supply and results in a more continuous wetted area during sliding. These observations support the role of the texture in facilitating lubricant release and replenishment under lubricant-starved conditions.

To better visualize and analyze the oil-extraction effectiveness of the texture, introduce image processing algorithms here to perform a quantitative analysis of the image results mentioned above. Here uses three parameters to evaluate secondary oil supply behavior on textured surfaces: lubrication area coverage ratio, mean gray value, and oil connectivity index (OCI). For details on the image

Just Accepted

processing and computational procedures, see Appendix B. A high coverage ratio indicates that the lubricant zones takes up a larger proportion of the entire interface area. A higher OCI value indicates that the detected lubricant is more concentrated in a single, major contiguous area, and that the oil trail exhibits greater overall continuity and fewer breaks.

The calculation results are shown in Table 4. Table 4 shows that the OCI gradually increased from near 0 at the initial time to approximately 0.55, reaching about 0.96 at 1915 ms, indicating that the lubricant trail gradually evolved from isolated distributions into a large-scale continuous region; At the same time, the lubrication coverage increased from near 0 at the initial time to approximately 19.13%, and further rose to about 63.81%, indicating that the effective coverage area of the lubricant on the friction surface continued to expand. The average gray value of the fixed region of interest (ROI) also gradually increased from approximately 123.13 to about 145.28, consistent with the trend of increasing lubricant film area and lubricant concentration on the surface. Combined with the oil trail migration phenomenon observed in high-speed cinematography, it can be argued that under the combined action of normal load and relative motion, the lubricant pre-stored within the textured structure gradually migrates toward the friction contact area and redistributes, thereby enhancing the coverage and spatial continuity of the lubricating oil film.

Table 4 **C**alculation results in Fig. 10

Figure	Time	OCI	Coverage ratio	Mean gray value
	0ms	0	0	123.13
Fig. 10a,c,d	366ms	0.55	19.13%	127.07
	1915ms	0.96	63.81%	145.28

Just Accepted

The results of the image calculations shown in Fig. 11 are presented in Table 5. For the smooth surface (Fig. 11a-d), the relative coverage of newly developed lubricant-related regions was 2.08% at 68 ms, decreased to 1.03% at 3106 ms, and subsequently increased to 5.57% at 3728 ms. The corresponding incremental OCI values were 0.27, 0.56, and 0.38, respectively. Meanwhile, the mean gray value initially decreased from 103.93 at 0 ms to 97.57-98.28 during the intermediate stages and then increased slightly to 106.49 at 3728 ms. These results indicate that lubricant redistribution occurred on the smooth surface during sliding; however, the newly developed lubricant regions remained relatively limited in spatial extent and exhibited only moderate connectivity, consistent with the discontinuous lubricant traces observed in Fig. 11d.

Table 5 Calculation results in Fig. 11

Figure	Time	OCI	Coverage ratio	Mean gray value
Fig. 11a-d	0ms	0	0	103.93
	68ms	0.27	2.08%	97.57
	3106ms	0.56	1.03%	98.28
	3728ms	0.38	5.57%	106.49
Fig. 11e-h	0ms	0	0	90.68
	632ms	0.47	1.51%	85.51
	3000ms	0.69	1.04%	83.82
	3609ms	0.71	21.46%	102.09

In contrast, the textured surface (Fig. 11e-h) exhibited a more pronounced redistribution of lubricant at the later stage of sliding. The relative coverage was 1.51% at 632 ms and 1.04% at 3000 ms, before increasing markedly to 21.46% at 3609 ms. At the same time, the incremental OCI increased

Just Accepted

from 0.47 to 0.69 and further to 0.71, indicating that the newly developed lubricant regions became progressively more connected. The mean gray value decreased from 90.68 at 0 ms to 85.51 and 83.82 during the intermediate stages, followed by a pronounced increase to 102.09 at 3609 ms. Compared with the smooth surface, the textured surface therefore produced a substantially larger and more spatially connected lubricant redistribution region at the final stage. This quantitative trend agrees with the visual observation in Fig. 11h, where a broad and continuous lubricant trace formed behind the sliding pin, supporting the role of the texture in promoting lubricant release, redistribution, and replenishment along the sliding interface.

3.3 Experimental results

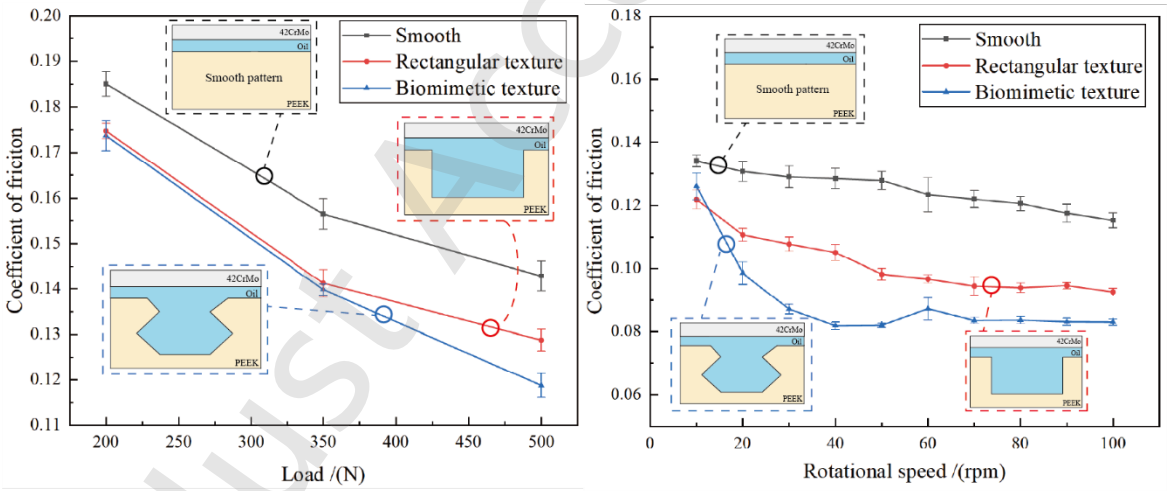
It is worth noting here that for any specific surface texture parameter, whether in experiments to determine load by adjusting rotational speed or to determine rotational speed by adjusting load, the experiments were conducted continuously without interruption; there was no change of lubricant, nor was the test bench or the specimen surface rinsed during the process. In the experimental results described below, for the load-determined speed adjustment test, the fixed load parameter was set to 500 N to simulate heavy-load conditions. For the speed-determined load adjustment test, the fixed speed parameter was set to 50 rpm, a midpoint value within the speed range that represents typical operating conditions. This avoids the instability caused by excessively high or low speeds, allowing the friction state to stabilize.

Each tribological test was independently repeated three times under the same operating conditions. Ensure that 0.1 mL of lubricant is entered on the interface, and that the texture is filled with lubricant. The friction coefficients shown are the averages of the three measurements, and the error bars represent the corresponding standard deviations.

Just Accepted

Figure 12 compares the friction-reduction performance of the biomimetic texture with those of the smooth and rectangular-textured surfaces under different normal loads and rotational speeds.

As shown in Fig. 12a, the coefficient of friction of the biomimetic-textured specimen was lower than those of the smooth and rectangular-textured specimens over the investigated load range. With increasing normal load, the friction coefficient of the biomimetic-textured specimen decreased progressively. At a load of 500 N, its friction coefficient was approximately 18% lower than that of the smooth specimen. This result indicates that the proposed biomimetic texture can effectively reduce friction under the investigated low-speed and heavy-load conditions. The improved frictional behavior may be attributed to load-induced deformation of the texture, which promotes lubricant release from the internal cavity and facilitates lubricant replenishment at the sliding interface during relative motion.



(a) Different load (b) Different rotational speed

Fig. 12 Friction properties of smooth surfaces, rectangular textures, and biomimetic textures.

As shown in Fig. 12b, the friction coefficients of both the biomimetic-textured and smooth specimens decreased with increasing rotational speed, whereas that of the rectangular-textured specimen remained relatively stable. Among the investigated surfaces, the biomimetic-textured specimen exhibited a comparatively lower friction coefficient over the tested speed range, demonstrating its friction-reduction capability under the investigated operating conditions.

Just Accepted

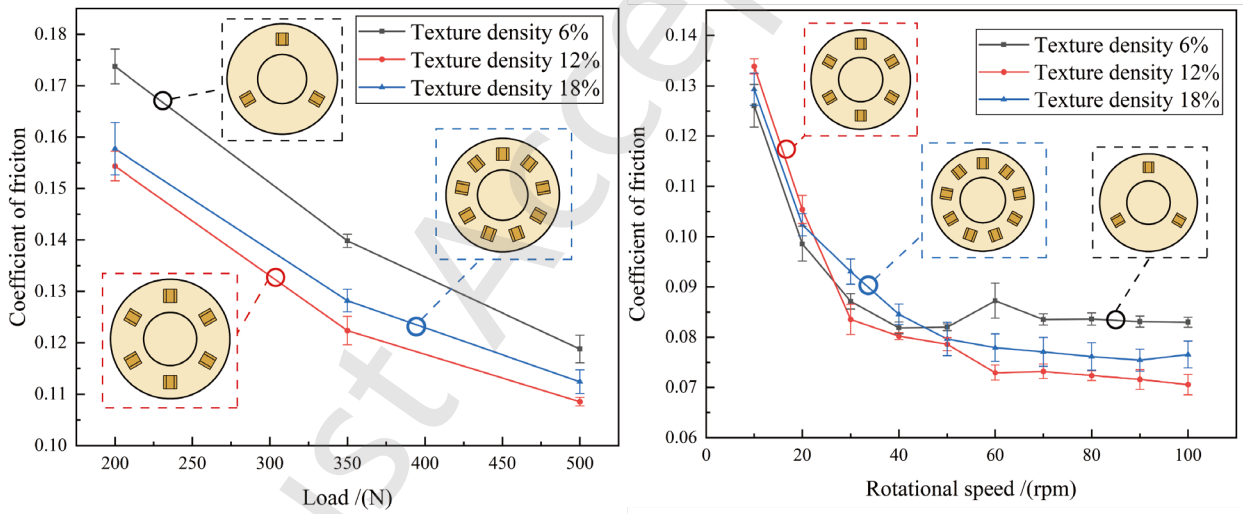
Surface texture generally exhibits an optimal areal density, and increasing the number of texture elements does not necessarily lead to improved tribological performance. To investigate the influence of texture density on the friction-reduction performance of the proposed biomimetic texture, friction and wear tests were conducted using specimens with the same texture geometry but different areal densities. The corresponding experimental results are presented in Fig. 13.

Figure 13a shows the influence of different texture density parameters on the texture anti-friction effect, aiming to explore the influence of the area proportion parameter of the texture area relative to the load-bearing area on the anti-friction effect. It can be seen from the figure that when the texture density is 6%, the curve shows the maximum coefficient of friction. As the density increases, the coefficient of friction curve shows a trend of first decreasing and then increasing. When the texture density is 12%, the experimental results show that the anti-friction effect is the best at this time. As shown in Fig. 13b, within the range where the rotational speed is lower than 60rpm, 6% of the texture patterns exhibit the smallest coefficient of friction, but at the same time, 11% and 18% of the texture patterns also show a significant decrease in the coefficient of friction.

At lower rotational speeds, a higher texture density reduces the effective load-bearing area of the contact surface and may consequently increase the local contact pressure and the extent of asperity interaction. Meanwhile, the amount of wear debris generated under these conditions is relatively limited. Therefore, the low-density textured surface exhibits comparatively favorable tribological performance at lower rotational speeds. When the rotational speed exceeds 60 rpm, the friction coefficients of the specimens with texture densities of 12% and 18% decrease further. At higher rotational speeds, increased sliding distance and interfacial interaction may lead to a greater accumulation of wear debris. For the specimen with a texture density of 6%, the relatively limited

Just Accepted

cavity volume provides insufficient capacity for debris accommodation, which may increase the likelihood of loose debris remaining at the sliding interface and participating in three-body abrasion, thereby weakening the friction-reduction effect. In contrast, although the 18% texture density provides greater lubricant storage and debris accommodation capacity, the excessive reduction in the effective load-bearing area and the dense distribution of texture elements may adversely affect lubricant redistribution across the contact interface. Consequently, the specimen with a texture density of 12% provides a more favorable balance among load-bearing capacity, lubricant replenishment, and debris accommodation, resulting in the lowest friction coefficient among the investigated texture densities at higher rotational speeds.



(a) Different load (b) Different rotational speed

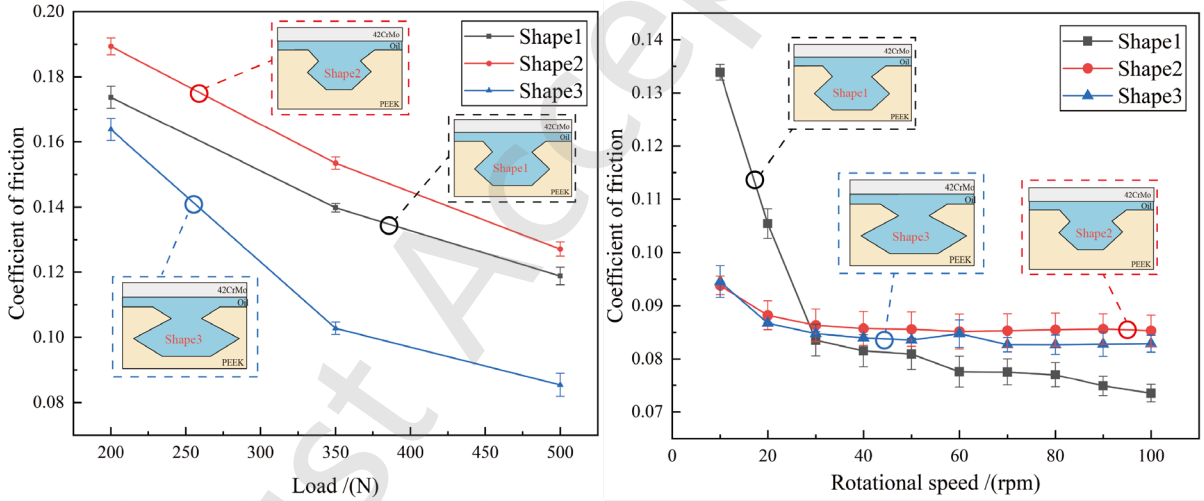
Fig. 13 Differences in wear reduction effects among various biomimetic texture density.

Figure 14a compares the friction-reduction performance of different texture geometries under varying normal loads. Among the investigated geometries, Shape1 exhibits the lowest coefficient of friction, whereas Shape3 shows the highest value. The differences in tribological performance are likely governed by the combined effects of lubricant storage, deformation-induced lubricant release, debris accommodation, and effective load-bearing area. Fig. 14b compares the frictional behavior of

Just Accepted

the different texture geometries at various rotational speeds. The coefficient of friction of Shape2 remains relatively stable over the investigated speed range. At lower rotational speeds, Shape3 exhibits the lowest coefficient of friction. However, when the rotational speed exceeds 30 rpm, Shape1 exhibits a lower coefficient of friction than Shape3.

The results in Fig. 14 suggest that the relative contribution of different lubrication mechanisms may vary with rotational speed. At lower rotational speeds, deformation-induced lubricant release may play a more important role, whereas at higher rotational speeds, lubricant storage, redistribution, and debris accommodation may become increasingly influential. This possible change in the dominant tribological mechanism is discussed further in Section 4.1.



(a) Different load (b) Different rotational speed

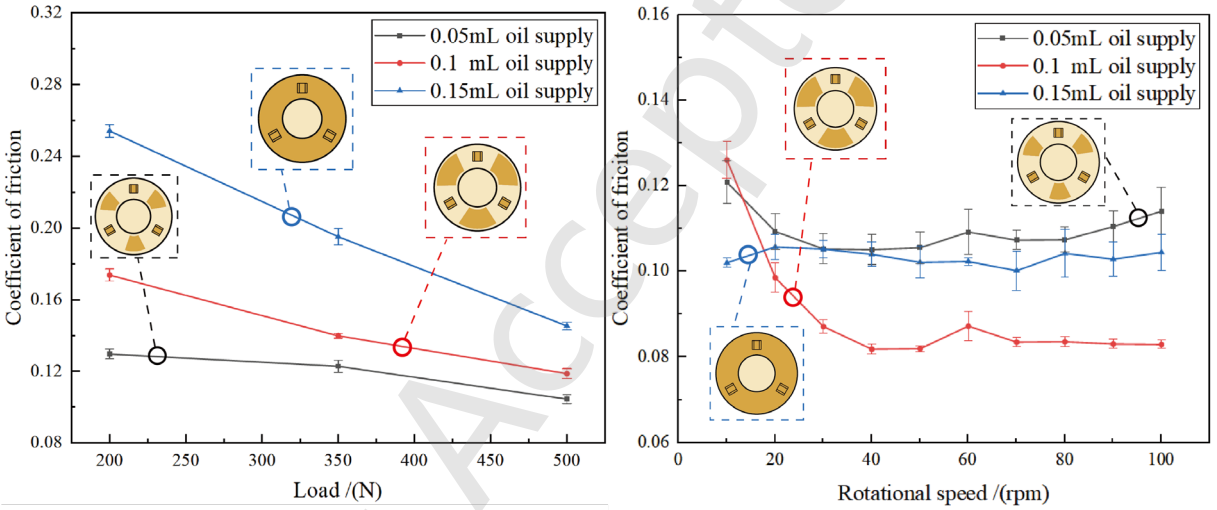
Fig. 14 Differences in wear reduction effects among various biomimetic texture shapes.

To investigate the influence of the initial lubricant supply on the friction-reduction performance of the textured surface, lubricant was first introduced into the texture cavities. Additional lubricant volumes of 0.05, 0.10, and 0.15 mL were then applied to the specimen surface, respectively. Friction tests were subsequently conducted under different normal loads and rotational speeds, and the corresponding results are presented in Fig. 15.

As shown in Fig. 15a, the coefficient of friction increases with increasing initial lubricant supply,

Just Accepted

whereas it generally decreases with increasing normal load. Fig. 15b presents the friction coefficients obtained under different initial lubricant volumes and rotational speeds. Under the investigated conditions, the specimens with a lower initial lubricant supply exhibit comparatively lower friction coefficients. Increasing the initial lubricant volume does not result in a further improvement in friction reduction, indicating a non-monotonic relationship between lubricant supply and tribological performance. The possible mechanisms responsible for this behavior are discussed in the following section.



(a) Different load (b) Different rotational speed

Fig. 15 Relationship between biomimetic texture anti-friction effect and surface oil supply.

4 Discussion

4.1 Mechanism discussion

The results obtained using the super-depth-of-field microscope are shown in Fig 16. Fig. 16a shows the surface of the non-textured region of the texture specimen before grinding, revealing distinct, disordered marks caused by sandpaper abrasion. Fig. 16b depicts the surface morphology of the non-textured region on the cephalopod-inspired textured specimen after abrasion. The image reveals

Just Accepted

relatively flat and uniform abrasion marks distributed across the surface, with no fine disordered scratches or deep, wide plow marks. The concave areas exhibit no significant height variations, indicating uniform wear distribution and a low degree of abrasion; Fig. 16c shows the post-friction image of the non-textured area on the rectangular textured surface. Clear, wide abrasion marks are visible, indicating severe plowing by abrasive particles or rough peaks in this region, with a higher degree of wear compared to the biomimetic textured surface; Fig. 16d displays the post-friction morphology of the smooth specimen surface, revealing extensive irregular deep scratches characteristic of severe friction abrasion.

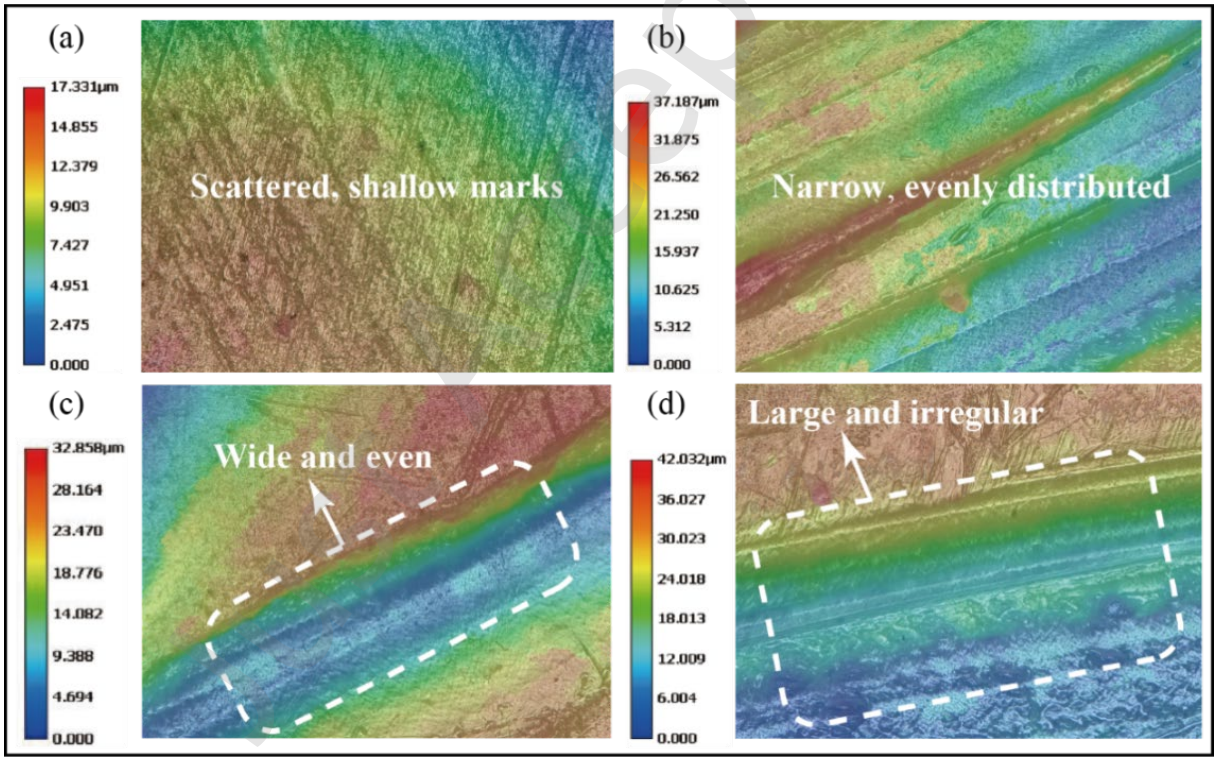


Fig. 16 Image after wear. (a) surface of the texture specimen before friction. (b) cephalopod texture pattern. (c) rectangular texture pattern. (d) smooth pattern.

Compared to the pre-friction surfaces, both the rectangle textured surface and the smooth surface exhibit noticeable friction marks. However, due to its excellent secondary lubrication effect and reservoir effect, the cephalopod-inspired textured surface shows the most uniform wear patterns

without wide grooves. This further validates the enhanced lubrication performance of the textured surface.

The mechanism of the textural reservoir can be invoked to explain the experimental results shown in Fig. 14. Shape3 with the maximum volume change rate does not exhibit the optimal tribological performance under different loads and different rotational speeds. The secondary lubrication related to volume change may not be the only dominant mechanism for reducing friction. As can be seen from Fig. 7, the surface of the textured PEEK sample tested by the friction experiment has a certain amount of black matter, and there is even more black matter inside the texture.

Under the test conditions of low-speed and heavy-load, as PEEK is a relatively soft engineering plastic material, PEEK chips will be produced when it is ground against metal samples. When the debris is not well handled and is driven to move between the two mating surfaces, the wear state between the working surfaces at this time is three-body wear, which will further deteriorate the friction state between the working surfaces. As shown in Fig. 7a, the black substance filled inside the texture proves that after the introduction of the texture structure, the unique reservoir effect of the texture has played a certain role. During the friction process, the internal concave feature of the texture can largely store PEEK wear debris, causing the surface friction state to change to two-body wear. This will improve the tribological properties of the surface and reduce the friction coefficient of the surface.

4.2 Limitations and future perspectives

Although this paper has verified the lubrication-enhancing effect of biomimetic textures under low-speed, heavy-load conditions through finite element analysis, high-speed photography, and friction and wear tests, several issues remain worthy of further study.

(1) A larger cavity volume contraction helps increase the potential discharge volume of the

Just Accepted

lubricant, but this does not necessarily imply a sustained improvement in lubrication performance. Excessive deformation may lead to localized stress concentration, cavity collapse, irreversible deformation, and a decrease in load-bearing capacity; therefore, in subsequent research, the degree of texture deformation should be treated as an optimization parameter rather than simply maximized. During unloading, the elastic recovery of the PEEK matrix causes the cavity volume to increase again and may create transient low pressure, thereby promoting the re-entry of lubricant into the cavity near the texture openings and forming a passive cycle characterized by "extrusion under load, recovery upon unloading, and local replenishment".

(2) As shown in Fig. 15, the lubricant supply quantity has a non-monotonic relationship with the friction performance. An appropriate amount of lubricant can reduce direct solid-solid contact. However, when the supply of lubricant is excessive, more lubricant will participate in the shear and entrainment processes within the contact area, which may increase viscous resistance and alter the local fluid dynamics interactions. This may partially offset the friction reduction effect. Therefore, the optimal lubrication state depends on the balance between solid-solid contact friction and fluid-related resistance. In the future, through oil film measurement and flow field analysis, the lubrication mechanism under different lubricant supply rates can be further clarified.

(3) This study primarily employs constant and step loads to verify the friction-reducing effect of the texture, whereas actual wind turbine sliding bearings are subjected to complex dynamic loads. Under high-frequency or random loads, the viscoelastic response of PEEK, lubricant viscosity, and outlet flow resistance may cause a time lag between structural deformation and lubricant transport; simultaneously, long-term cycling may also lead to residual deformation, fatigue, and lubricant dissipation. Therefore, future experimental studies will be conducted under cyclic, random, and actual

Just Accepted

load spectrum conditions.

(4) The biomimetic concept presented in this paper falls under functional biomimetic rather than a direct mechanical equivalence between the lateral contraction of biological ink sacs and the normal loads on engineered textures. The narrow-neck and large-cavity structure achieves lubricant release through the synergistic effects of localized concentrated deformation and oil-storage capacity; however, low local stiffness alone does not guarantee greater cavity contraction, as its effect still depends on the overall geometric parameters and the direction of deformation. In future studies, a single-factor parameterization method could be employed to further investigate the independent effects of neck width, cavity depth, and sidewall angle on volumetric contraction ratio, structural stress, and lubricant delivery capacity.

5 Conclusions

This study focuses on the working interface of PEEK-coated wind turbine sliding bearings, which are characterized by low-speed, heavy-load operating conditions and a substrate prone to significant deformation. Drawing inspiration from the ink sac structure of marine cephalopods, a novel biomimetic textured structure was designed. The results demonstrate that the tribological performance of the biomimetic textured surface is governed by the coupled effects of lubricant storage, deformation-induced lubricant release, lubricant replenishment, and debris accommodation, rather than by a single geometric parameter.

(1) Compared with smooth surfaces, the biomimetic texture reduced the coefficient of friction by 18% under the lowest rotational speed and heaviest loads, confirming that the introduction of internal lubricant reservoirs can effectively improve lubrication under low-speed and heavy-load

Just Accepted

conditions.

(2) Among the three texture geometries, Shape1 exhibited the best overall tribological performance. This result suggests that maximizing cavity deformation or lubricant-release capacity alone does not necessarily lead to the lowest friction; instead, an appropriate balance between lubricant replenishment and debris-retention capability is required to maintain a stable interfacial lubrication state.

(3) The optimum texture coverage of 12% reflects a compromise between increasing the effective lubricant-storage capacity and preserving sufficient load-bearing area of the PEEK surface.

(4) The initial lubricant supply also exhibited a non-monotonic influence: an oil volume of 0.05 mL produced the most favorable lubrication behavior, indicating that excessive lubricant supply does not necessarily further reduce friction and may alter the interfacial flow state and increase viscous shear losses.

(5) The super-depth-of-field microscopy results show that the biomimetic textures reduce the width of the scuff marks and promote a more uniform wear distribution, indicating mitigation of severe localized contact and surface damage.

(6) High-speed imaging directly reveals the migration of lubricant from the internal texture cavities toward the sliding interface under normal loading and relative motion, providing experimental evidence for the deformation-induced lubricant-release and replenishment process.

These results indicate that the effectiveness of the proposed biomimetic texture arises from the coordinated regulation of lubricant storage, controlled release, interfacial replenishment, debris accommodation, and load-bearing capacity. Therefore, the design of textured PEEK surfaces should not pursue the maximum cavity volume, deformation, or lubricant supply independently, but should

Just Accepted

instead optimize their coupled relationship according to the applied load, sliding speed, and lubrication condition. This finding provides a mechanistic basis and engineering design principles for polymer surfaces that function under low-speed, high-load conditions, and is significant for bearing interfaces used in wind energy systems.

Appendix A

Calculate the minimum oil film thickness according to the above Formula.4, the formula for Composite radius R：

$$\frac{1}{R}=\frac{1}{R_{\mathrm{a}}}+\frac{1}{R_{\mathrm{b}}} \tag{A.1}$$

Radius of the metal pin R_{a}=2mm, Operating radius of the metal pin R_{b}=25mm. Elipticity parameter k=1. η=0.047Pa·s, mean velocity u=(u_{PEEK}+$u_{42\mathrm{CrMo}}$)/2=0.045m/s , elastic modulus of metal pins $E_{42\mathrm{CrMo}}$=210GPa, poisson ratio $\upsilon_{42\mathrm{CrMo}}$=0.3. Elastic modulus of PEEK E_{PEEK}=2GPa, poisson ratio υ_{PEEK}=0.4. Applied external load F_{N}=200N. σ_{PEEK}=3.2mm, $\sigma_{42\mathrm{CrMo}}$=1.6mm. Calculated film thickness ratio parameter λ<1. It can be determined that the lubrication condition in this document is in a boundary lubrication state.

Appendix B

The OCI index is defined as:

$$OCI(t)=\frac{\max\left\{A_1,A_2,\cdots,\ A_{\mathrm{N}}\right\}}{\sum_{j=1}^{N}A_{\mathrm{j}}} \tag{B.1}$$

Where A_1-A_N are the areas of N independent oil stains.

The coverage ratio at time t is defined as:

Just Accepted

$$C(t) = \frac{A_{\text{oil}}(t)}{A_{\text{eff}}(t)} \times 100\% \tag{B.2}$$

The total number of valid pixels included in the coverage calculation is determined by the following formula:

$$A_{\text{eff}}(t) = \sum_{x,y} V_{\text{t}}(x,y) \tag{B.3}$$

The total lubrication zones at different times is calculated using the following formula:

$$A_{\text{oil}}(t) = \sum_{x,y} M_{\text{t}}(x,y) \tag{B.4}$$

The lubricant zone is determined using the following formula:

$$M_{\text{t}}(x,y) = \begin{cases} 1, & \Delta I_{\text{t}}(x,y) > \Delta T \\ 0, & \Delta I_{\text{t}}(x,y) \le \Delta T \end{cases} \tag{B.5}$$

Where ΔT is the set gray increment threshold，$M_{\text{t}}(x,y)$ is the binary mask for the lubricant，When the value of M_{t} is 1, this zone is defined as the lubricant zone.

To calculate the grayscale increment of a pixel at 0ms relative to different points in time, use the following formula:

$$\Delta I_{\text{t}}(x,y) = I_{\text{t}}^{\text{f}}(x,y) - I_{0}^{\text{f}}(x,y) \tag{B.6}$$

Where (x,y) is the pixel coordinates in the image，$I_{0}^{\text{f}}(x,y)$ is the grayscale value of the 0 ms image after filtering，$I_{\text{t}}^{\text{f}}(x,y)$ is the gray value of the image after filtering at time t.

Since during the image registration process, there is probability that the image edges will have black borders that do not contain any real image information, therefore, after image registration, an effective region mask needs to be defined:

$$V_{\text{t}}(x,y) = \begin{cases} 1, & \text{Pixels belong to the valid analysis area} \\ 0, & \text{Pixel is not part of the valid analysis area} \end{cases} \tag{B.7}$$

The same image processing methods were used for both the time-resolved analysis of lubricant migration and the comparison between smooth and textured surfaces. The images were cropped to the

Just Accepted

same field of view. They were converted to grayscale images in MATLAB, spatially registered, and smoothed using a Gaussian filter to remove noise. The 0ms image for each sample served as the reference frame, after which the difference in grayscale values between each subsequent frame and its reference image was calculated. A uniform threshold was then applied to generate a binary lubricant distribution map, from which the coverage ratio, mean grayscale change, and OCI were calculated.

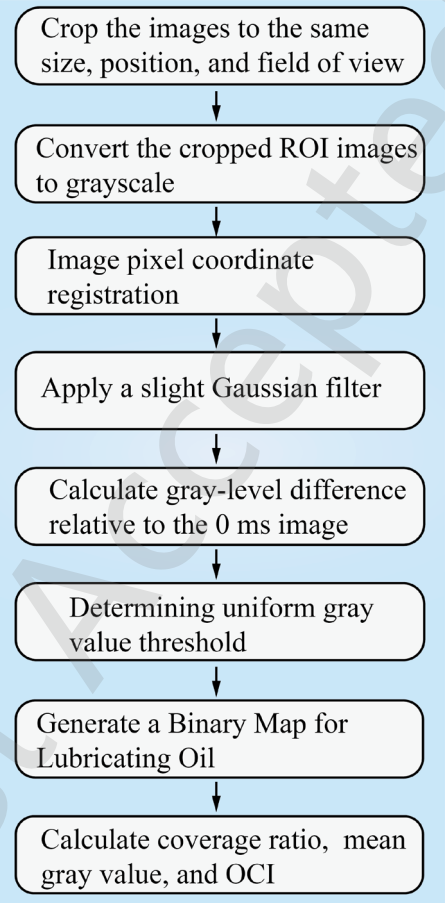


Fig. B1 Flowchart of image processing.

Here, taking Fig. 10 as an example, the image segmentation results and the calculation results of the final three parameters are presented.

Just Accepted

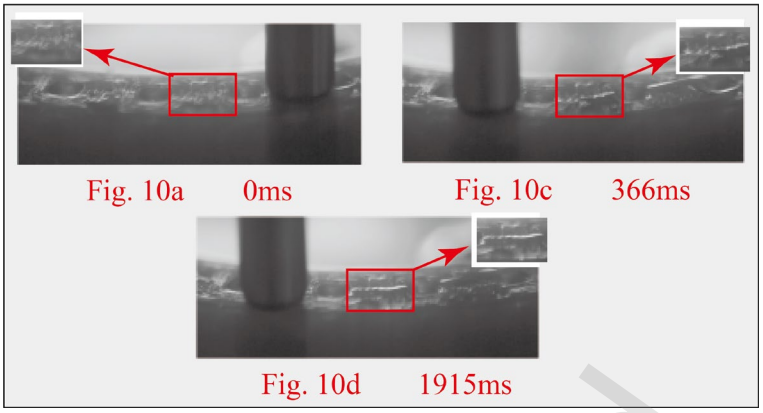


Fig. B2 Selection of the ROI area in Fig. 10.

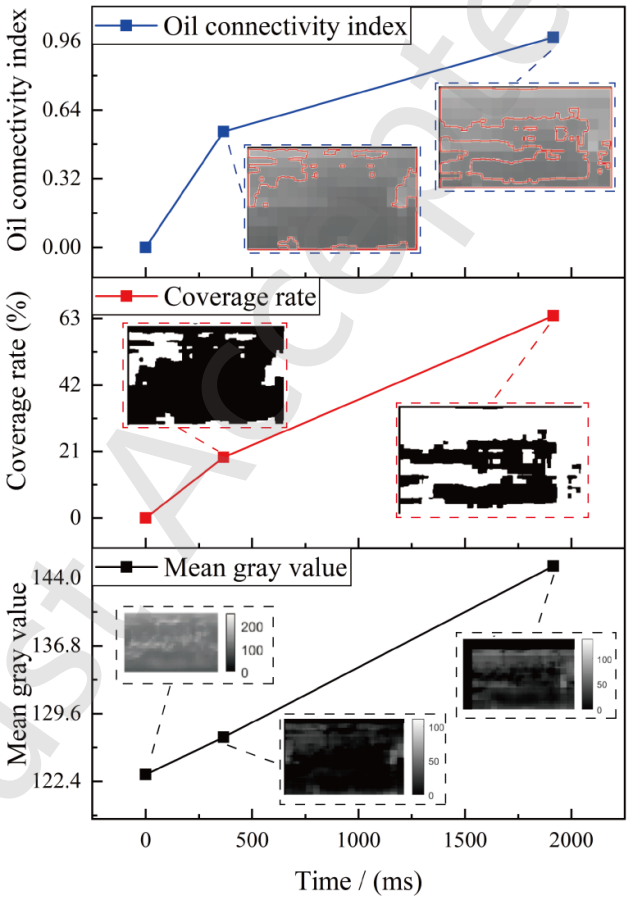


Fig. B3 Mean gray values, coverage ratio, and OCI calculation results in Fig. 10.

Just Accepted

Acknowledgements

This work was supported by National Science and Technology Major Project of China(Grant No. 2024ZD0705501).

Funding

The first and corresponding authors would like to acknowledge the financial support from the National Science and Technology Major Project of China(Grant No. 2024ZD0705501).

Author contributions

All authors contributed to the study conception and design. Material preparation and analysis were performed by Junyang Shang, Chengxu Zhang and Tianyi Tang. The first draft of the manuscript was written by Junyang Shang, and all authors commented on previous versions of the manuscript, especially Kai Feng and Kai Zhang. All authors read and approved the final manuscript.

Availability of data and materials

The data that support the findings of this study can be downloaded from the corresponding author upon reasonable request.

Declarations of competing interest

The authors have no competing interests to declare that are relevant to the content of this article.

Just Accepted

References

[1] Zhang K, Hu X L, Zheng G L, Liu L S, Chu X C, Wu X Y, Feng K. Thermo-elastohydrodynamic performance of sliding main bearings in wind turbines: Numerical and experimental investigation. *Tribol Int* **216**: 111481 (2025) https://doi.org/10.1016/j.triboint.2025.111484.

[2] Cheng S, Meng X H, Yin J B , Yang L, Zhang Z J. Configuration performance of main shaft bearings for transient-loaded wind turbine. *International Journal of Mechanical Sciences* **293**: 110171 (2025) https://doi.org/10.1016/j.ijmecsci.2025.110171.

[3] Wang L T, Cai J R, Ding X K, Wang Z H, Wang X. Multidisciplinary design and optimization of journal bearing for high-power wind turbine speed increaser. *Tribol Int* **197**: 109765 (2024) https://doi.org/10.1016/j.triboint.2024.109765.

[4] Xia S Q, Huang C, Ye S G, Jiao W X, Xia Y, M Zhu Z M. Study on the running-in tribological performance and mechanism of the valve plate with surface texture for axial piston pumps. *Wear* **574**–**575**: 206805 (2025) https://doi.org/10.1016/j.wear.2025.206085.

[5] Xiao Q H, Wang X Y, Wang Y Y, Zheng W, Xu J W, Luo X C, Sun J N, Zhang L. Beyond smoothness: the art of surface texturing battling against friction. *Int Journal Extreme Manuf* **7**(2): 022014 (2025) https://doi.org/10.1088/2631-7990/ad9c01.

[6] Lian Z X, Zhou J H, Ren W F, Chen F Z, Xu J K, Tian Y L, Yu H D. Recent progress in bio-inspired macrostructure array materials with special wettability—from surface engineering to functional applications. *Int J Extreme Manuf* **6**: 012008 (2023) https://doi.org/10.1088/2631-7990/ad0471.

[7] Zhang J R, Yu T, Lu L B. Laser Surface Texturing for Tribological Applications: Mechanisms,

Just Accepted

Surface Engineering Strategies, and Application-Oriented Design. *Lubricants* **14**(6): 239 (2026) https://doi.org/10.3390/lubricants14060239.

[8] Long R S, Wang H M, Hou J C, Shang Q Y, Zhang Y M, Zong L, Zhang Z J. Tribological behavior of the laser Micro-Textured PEEK-1040 steel friction pairs. *Polymers* **17**(5): 645 (2025) https://doi.org/10.3390/polym17050645.

[9] Zhang Y L, Zhang X G, Matsoukas G. Numerical study of surface texturing for improving tribological properties of ultra-high molecular weight polyethylene. *Biosurf Biotribol* 2015, **1**(4): 270-277 (2015) https://doi.org/10.1016/j.bsbt.2015.11.003.

[10] Chang T, Guo Z W, Yuan C Q. Study on influence of Koch snowflake surface texture on tribological performance for marine water-lubricated bearings. *Tribol Int* **129**: 29-37 (2019) https://doi.org/10.1016/j.triboint.2018.08.015.

[11] Li S J, Wu Z P, Dong B W, Luo W Y, Song H L, Guo H T, Zhou Q Q. Improvement of lubrication performance of sliding pairs with multi-depth groove textures based on genetic algorithm. *Surf Topogr-Metrol Prop* **11**(2): 025011 (2023) https://doi.org/10.1088/2051-672X/acd46a.

[12] Vignesh G, Barik D, Sharma P, Medhi B J, Bora B J. Numerical investigation and optimization of the geometric profiles of dimple bottom structure in frictional interaction pairs. *Tribol Int* **185**: 108530 (2023) https://doi.org/10.1016/j.triboint.2023.108530.

[13] Zhang H., Zhang D Y, Hua M, Dong G N, Chin K S. A Study on the Tribological Behavior of Surface Texturing on Babbitt Alloy under Mixed or Starved Lubrication. *Tribol Lett* **56**: 305–315 (2014) https://doi.org/10.1007/s11249-014-0410-4.

[14] Aher V S, Shirsat U M, Wakchaure V D, Venkatesh M A. An experimental investigation on tribological performance of UHMWPE composite under textured dry sliding conditions. *J Tribol* **24**:

Just Accepted

110-125 (2020).

[15] Jin Z Y, Zhang X F, Hou Z B, Yao Z Q, Shen H. Tribological Properties of Carbon Fiber-Reinforced PEEK against 304 Stainless Steel with Reticulate Surface Texture. *Materials* **15**(24): 8789 (2022) https://doi.org/10.3390/ma15248789.

[16] Chen Y, Xu, P, Yu, Y H, Shen J X. Optimization of Laser-Induced Composite Micro-Textures on PEEK/CF Composites and Their Wetting-Friction Behaviors. *Lubricants* **13**(12): 538 (2025) https://doi.org/10.3390/lubricants13120538.

[17] Liu Y, Zhang H, Dai S J, Dong G N. Designing a bioinspired scaly textured surface for improving the tribological behaviors of starved lubrication. *Tribol Int* **173**: 107594 (2022) https://doi.org/10.1016/j.triboint.2022.107594.

[18] Harris C W, Doustdar O, Taghizadeh Tabrizi A, Al-Qahtani A M, Hajiyavand A M, Dearn K D. Hydrodynamic lubrication effects in textured PEEK surfaces for friction reduction. *Discov Mech Eng* **4**(1): 41 (2025) https://doi.org/10.1007/s44245-025-00130-6.

[19] Wang M L. The tribological performance of engineered micro-surface topography by picosecond laser on PEEK. *Ind Lubr Tribol* **72**(1):172-179 (2020) https://doi.org/10.1108/ILT-06-2019-0202.

[20] Yuan S, Lin N M, Wang W H, Zhang H X, Liu Z Q, Yu Y, Zeng Q F, Wu Y C. Correlation between surface textural parameter and tribological behaviour of four metal materials with laser surface texturing (LST). *Appl Surf Sci* **583**: 152410 (2022) https://doi.org/10.1016/j.apsusc.2021.152410.

[21] Narayana T, Saleem S S. Enhancing fretting wear behavior of Ti64 alloy: The impact of surface textures and CrN-MoS2-Ag composite coating. *Tribol Int* **193**: 109346 (2024) https://doi.org/10.1016/j.triboint.2024.109346.

[22] Gheisari R, Lan P, Polycarpou A A. Efficacy of surface microtexturing in enhancing the

Just Accepted

tribological performance of polymeric surfaces under starved lubricated conditions. *Wear* **444**: 203162 (2020) https://doi.org/10.1016/j.wear.2019.203162.

[23] Su B B, Zou X G, Wang Z X, Huang L R. Numerica2l analysis of lubrication properties on a bio-inspired parabolic textured surface. *Meccanica* **59**(6): 987-1000 (2024) https://doi.org/10.1007/s11012-024-01838-7.

[24] Wang Z Q, Fu Q, Wood R J K, Wu J, Wang S C. Influence of bionic non-smooth surface texture on tribological characteristics of carbon-fiber-reinforced polyetheretherketone under seawater lubrication. *Tribol Int* **144**: 106100 (2020) https://doi.org/10.1016/j.triboint.2019.106100.

[25] Hanlon R T, Messenger J B. *Cephalopod behaviour*. Cambridge (UK): Cambridge University Press, 2018. https://doi.org/10.1017/9780511843600.

[26] Bush S L. Defensive behaviors of deep-sea squids: Ink release, body patterning, and arm autotomy. Ph.D. Thesis. California (The United States): University of California, 2009 https://escholarship.org/uc/item/526816j9.

[27] Derby C D. Cephalopod ink: production, chemistry, functions and applications. *Mar Drugs* **12**(5): 2700-2730 (2014) https://doi.org/10.3390/md12052700.

[28] Bartol I K, Krueger P S, Stewart W J, Thompson J T. Hydrodynamics of pulsed jetting in juvenile and adult brief squid Lolliguncula brevis: evidence of multiple jetmodes' and their implications for propulsive efficiency. *J Exp Biol* **212**(12): 1889-1903 (2009) https://doi.org/10.1242/jeb.027771.

[29] Jiang M W, Zhao C X, Yan R X, Li J P, Song W W, Peng R B, Han Q X, Jiang X M. Continuous inking affects the biological and biochemical responses of cuttlefish Sepia pharaonis. *Front Physiol* **10**: 1429 (2019) https://doi.org/10.3389/fphys.2019.01429.

[30] Nair R J, Pillai D, Joseph S M, Gomathi P, Senan P V, Sherief P M. Cephalopod research and

Just Accepted

bioactive substances. *Indian J Mar Sci* **40**(1): 13-27 (2011) https://rgcb.sciencecentral.in/id/eprint/579.

[31] Gestal C, Pascual S, Guerra A, Fiorito G, Vieites J M. *Handbook of pathogens and diseases in cephalopods*. Cham (Switzerland): Springer, 2019. https://doi.org/10.1007/978-3-030-11330-8.

[32] Kouediatouka A N, Ma Q, Liu Q, Mawignon F J, Rafique F, Dong G N. Design methodology and application of surface texture: A review. *Coatings* **12**(7): 1015 (2022) https://doi.org/10.3390/coatings12071015.

[33] Shahrubudin N, Lee T C, Ramlan R. An overview on 3D printing technology: Technological, materials, and applications. *Procedia Manuf* **35**: 1286-1296 (2019) https://doi.org/10.1016/j.promfg.2019.06.089.

[34] Buchanan C, Gardner L. Metal 3D printing in construction: A review of methods, research, applications, opportunities and challenges. *Eng Struct* **180**: 332-348 (2019) https://doi.org/10.1016/j.engstruct.2018.11.045.

[35] Duda T, Raghavan L V. 3D metal printing technology. *IFAC-Pap* **49**(29): 103-110 (2016) https://doi.org/10.1016/j.ifacol.2016.11.111.

[36] Raina A, Anand A. Tribological investigation of diamond nanoparticles for steel/steel contacts in boundary lubrication regime. *Appl Nanosci* **7**(7): 371-388 (2017) https://doi.org/10.1007/s13204-017-0590-y.

Just Accepted

Junyang Shang.
He is currently working toward the Ph.D. degree in Mechanical Engineering with the School of Hunan University, Changsha,China, His research interests include wear-resistant surface materials, surface modification, biomimetic surface textures, and sliding bearings for wind turbines.



Tianyi Tang.
He received the B.S.degree in Mechanical Design, Manufacturing, and Automation from Chang'an University, Xi'an, China in 2020 and the M.S.degree in Mechanical Engineering from Hunan University, Changsha,China in 2023.

He is currently working toward the Ph.D. degree in Mechanical Engineering with the School of Hunan University, Changsha,China, His research interests include Multi-scale, Polymer composite materials and Wind turbine sliding main bearings.



Kai Zhang.
He studied at the School of Mechanical Engineering of Xi'an Jiaotong University from 2010 to 2017, and obtained his doctoral degree from Xi'an Jiaotong University in 2017. Now he is a professor at Hunan University.

His research specialties include friction, wear and lubrication, digital twin design and manufacturing of new transmission chains for large wind turbine generators, as well as intelligent detection of operating status.



Just Accepted